Precursors_cci+

ESA Climate Change Initiative (CCI)



D5.1 Climate Assessment Report version 2 (CAR_v2)

Title	D5.1 Climate Assessment Report (CAR)
Reference	Precursors_cci+_D5.1_CAR_02_05
Issue	02
Revision	05
Status	Draft
Date of issue	28/05/2026
Document type	Deliverable

This work has received funding from the European Space Agency under Contract No 4000138243 and is the result of the cooperation between the partners of the Precursors_cci+ consortium.















Generated by BIRA-IASB

	FUNCTION	NAME	DATE
LEAD AUTHOR(S)	Scientists	Herizo Narivelo Brice Barret Folkert Boersma Beata Opacka Glenn-Michael Oomen Jenny Stavrakou Jean-François Müller Maya George Selviga Sinnathamby Cathy Clerbaux	08/09/2025 8/10/2025 6/10/2025
REVIEWED BY	Science Leaders	M. Van Roozendael Folkert Boersma	02/01/2026 02/01/2026
	ESA Project Officer	Simon Pinnock	../../….
DISTRIBUTED TO	ESA Precursors_cci+ Consortium		

DOCUMENT CHANGE RECORD

Issue	Revision	Date	Modified items	Observations
1	0	03/04/2024	Initial template	Creation of document
1	2	23/04/2024	First draft	
1	3	03/06/2024	Revision following RIDs	
2	1	08/09/2025	Draft of GEOSCHEM part	
2	2	08/10/2025	Draft of MAGRITTE part	
2	3	20/12/2025	Creation of integrated document containing all parts	
2	4	02/01/2026	Addition of section on CO intercomparisons	
2	5	28/05/2026	Revision following ESA RIDS	

Table of Contents

1. PURPOSE AND SCOPE 5

1.1. Purpose 5

1.2. Scope 5

1.3. Applicable documents 5

1.4. Reference documents 5

1.5. List of acronyms 6

2. EVALUATION OF NO_2 AND CO CLIMATE DATA RECORDS FOR ECMWF CAMS 9

2.1. Status of assimilation of satellite NO_2 in CAMS re-analysis 9

2.2. Status of assimilation of satellite CO in CAMS re-analysis 10

2.3. Perspective of assimilation of satellite HCHO in CAMS re-analysis 11

3. GEOS-CHEM SIMULATIONS WITH CONSTRAINTS FROM HCHO AND NO_2 CLIMATE DATA RECORDS 11

3.1. Executive summary 11

3.2. General objectives and motivation 12

3.3. Satellite datasets 13
3.3.1. OMI and TROPOMI satellite observations 13
3.3.2. IASI-SOFRID data 13

3.4. GEOS-Chem model overview, simulation setup and strategy of the model assessment 14
3.4.1. GEOS-Chem model overview 14
3.4.2. Setup of the reference's simulations 15
3.4.3. Strategy of model assessment and choice of the reference simulations 15

3.5. Results and interpretations 17
3.5.1. Assessment of the GEOS-Chem simulations with the satellite data 17
3.5.2. Bias analysis 18
3.5.3. Taylor Diagram analysis 20
3.5.4. Global distributions of ozone and its precursors 22
3.5.5. Global ozone trends over 2008 -2020 period 24
3.5.6. Conclusion and perspectives 26

4. ASSESSMENT OF THE VARIABILITY AND TRENDS OF HCHO COLUMNS OVER AFRICA 26

4.1. Executive summary 26

4.2. Introduction 27

4.3. Satellite OMI formaldehyde observations 28

4.4. MAGRITTE model and simulation setup 28
4.4.1. MAGRITTE CTM 28
4.4.2. Model setup and simulations 29

4.5. Results and interpretation 30
4.5.1. Average HCHO columns, variability and trends 30
4.5.2. Contributions to HCHO columns from individual sources 35
4.5.3. Sensitivity analysis: Biomass burning VOC and soil NO inventories 38

4.6. Conclusion and perspectives 41

5. IASI/MOPITT/TROPOMI CO TOTAL COLUMN COMPARISON 41

5.1. Introduction and context 41

5.2. Timeseries over different latitude bands 43

5.3. Seasonal comparison 45

5.4. Regional trend analysis 47

5.5. Summary of Antje Inness ACP paper: Assimilation of S5P/TROPOMI carbon monoxide data with the global CAMS near-real-time system (2022) 50

5.6. Conclusion 51

6. REFERENCES 52

1. Purpose and scope

1.1. Purpose

This document presents the second issue of the Climate Assessment Report for cycle 2 of the ESA CCI+ ECV Precursor project.

1.2. Scope

The scope of this CAR_v2 is to report on lessons learned on using long-term satellite NO_2, HCHO and CO (generated within this project) at ECMWF CAMS, the University of Toulouse (LAERO) and BIRA-IASB for the purpose of climate assessment. This involves features of availability, coverage, consistency, completeness, uncertainty (propagation), and validation of the satellite data, and its usefulness for comparison against model simulations at timescales at which the climate, or aspects thereof, are noticeably changing.

Three main use cases are being developed addressing respectively (1) the evaluation of NO_2 and CO climate data records for ECMWF CAMS, (2) GEOS-CHEM simulations constrained by HCHO and NO_2 climate data records, and (3) the assessment of the variability and trends of HCHO columns over Africa. In addition, the CAR_v2 includes an intercomparison of CO column measurements from the IASI, MOPPIT and TROPOMI instruments, which concludes on the complementarity between these sensors for global CO monitoring.

1.3. Applicable documents

[AD-1] Data Standards Requirements for CCI Data Producers. Latest version at time of writing is v1.2: ref. CCI-PRGM-EOPS-TN-13-0009, 9 March 2015, available online at: https://climate.esa.int/media/documents/CCI_DataStandards_v2-3.pdf

[AD-2] CCI Data Policy v1.1. Available online at: https://climate.esa.int/sites/default/files/CCI_Data_Policy_v1.1.pdf

1.4. Reference documents

[RD-1] GCOS Climate Monitoring Principles, November 1999. Available online at: https://gcos.wmo.int/en/essential-climate-variables/about/gcos-monitoring-principles

[RD-2] Guideline for the Generation of Satellite-based Datasets and Products meeting GCOS Requirements, GCOS Secretariat, GCOS-128, March 2009 (WMO/TD No. 1488). Available online at: https://library.wmo.int/index.php?lvl=notice_display&id=12884#.Yw4rL7RByUk

[RD-3] Quality assurance framework for earth observation (QA4EO): http://qa4eo.org

[RD-4] The Global Observing System for Climate: Implementation Needs, GCOS-200, October 2016. Available online at: https://gcos.wmo.int/en/gcos-implementation-plan

[RD-5] Status of the Global Observing System for Climate, GCOS-195, October 2015. Available online at: https://library.wmo.int/index.php?lvl=notice_display&id=18962#.Yw4r8LRByUk

[RD-6] Hollmann, R., et al., The ESA climate change initiative: Satellite data records for essential climate variables. American Meteorological Society. Bulletin, Vol. 94, No. 10, 2013, p. 1541-1552.

[RD-7] Joint Committee for Guides in Metrology, 2008, Evaluation of measurement data — Guide to the expression of uncertainty in measurement (GUM), JGCM 100: 2008. Available online at: https://www.iso.org/sites/JCGM/GUM-JCGM100.htm

[RD-8] Merchant, C., et al., 2017, Uncertainty information in climate data records from Earth observation, Earth Syst. Sci. Data Discuss., vol. 9, p511-527

1.5. List of acronyms

AC-SAF	Satellite Application Facility on Atmospheric Composition Monitoring
ADP	Algorithm Development Plan
AK	Averaging Kernel
AMF	Air-mass factor
AOD	Aerosol Optical Depth
ATBD	Algorithm Theoretical Basis Document
BB	Biomass-Burning
BB	Biomass-Burning
BIRA-IASB	Royal Belgian Institute for Space Aeronomy
BIRA-IR	BIRA-IASB Infrared Team
BIRA-MOD	BIRA-IASB Tropospheric Modeling Team
BIRA-SYN	BIRA-IASB Synergy Team
BIRA-UVVIS	BIRA-IASB UV-Vis Team
BU	Bottom-Up
BVOCs	Biogenic Volatile Organic Compounds
C3S	Copernicus Climate Change Monitoring Service
C_5H_8	Isoprene
CAMS	Copernicus Atmospheric Monitoring Service
CCI	Climate Change Initiative
CCI+	Climate Change Initiative Extension (CCI+), is an extension of the CCI over the period 2017-2024.
CEDS	Community Emissions Data System
CEOS	Committee on Earth Observation Satellites
CH_4	Methane
CMUG	Climate Modeling User Group
CO	Carbon monoxide
COBRA	COvariance-Based Retrieval Algorithm
CRDP	Climate Research Data Package
CRG	Climate Research Group

CTM	Chemistry Transport Model
DLR	German Aerospace Centre
DOAS	Differential Optical Absorption Spectroscopy
ECMWF	European Centre for Medium-range Weather Forecast
ECV	Essential Climate Variable
ENVISAT	Environmental Satellite (ESA)
EO	Earth Observation
EQAS	Equatorial Asia
ESA	European Space Agency
EU	European Union
EUMETSAT	European Organisation for the Exploitation of Meteorological Satellites
FCDR	Fundamental Climate Data Record
FINN	Fire INventory from NCAR
FRESCO	Fast Retrieval Scheme for Clouds from the Oxygen A band
FRM	Fiducial Reference Measurement
FRP	Fire Radiative Power
GCHP	GEOS-Chem High Performance
GCOS	Global Climate Observation System
GEOS-Chem	Goddard Earth Observing System Chemistry
GFED	Global Fire Emissions Database
GOME	Global Ozone Monitoring Instrument (aboard ERS-2)
GOME-2	Global Ozone Monitoring Instrument – 2 (aboard MetOp-A, -B and -C)
HEMCO	Harvard-NASA Emissions Component
HRI	Hyperspectral Range Index
IASI	Infrared Atmospheric Sounding Interferometer
ICZ	Intertropical Convergence Zone
IGAC	International Global Atmospheric Chemistry
IUP-UB	Institute of Environmental Physics, University of Bremen
KNMI	Royal Netherlands Meteorological Institute
LAERO	Laboratoire d'Aérologie
LCC	Land Cover Changes
LEO	Low Earth Orbit
LUT	Look-up table
MEGAN	Model of Emissions of Gases and Aerosols from Nature
MERRA	Modern-Era Retrospective analysis for Research and Applications
Metop	Meteorological Operational Platform (EUMETSAT)
MOPITT	Measurement of Pollution in the Troposphere
NASA	National Aeronautics and Space Administration
NDACC	Network for the Detection of Atmospheric Composition Change
NH_3	Ammonia
NHAF	Northern Hemisphere Africa
NMVOCs	Non-Methane Volatile Organic Compounds
NN	Neural Network
NO	Nitrogen monoxide
NO_2	Nitrogen dioxide

NOx	Nitrogen oxides
NRT	Near-Real Time
O_3	Ozone
OCRA	Optical Cloud Recognition Algorithm)
OH	Hydroxyl Radical
OMI	Ozone Monitoring Instrument (aboard EOS-Aura)
PBL	Planetary Boundary Layer
PCA	Principal Component Analysis
QA4ECV	Quality Assurance for Essential Climate Variables
QA4EO	Quality Assurance framework four Earth Observation
QFED	Quick Fire Emissions Dataset
R&D	Research and Development
ROCINN	Retrieval of Cloud Information using Neural Networks
S5P	Sentinel-5 Precursor
SAF	Satellite Application Facility
SCIAMACHY	Scanning Imaging Absorption Spectrometer for Atmospheric
SEAS	Southeast Asia
SHAF	Southern Hemisphere Africa
SHSA	Southern Hemisphere South America
SOA	Secondary Organic Aerosols
SOFRID	SOftware for a Fast Retrieval of IASI Data
SoW	Statement of Work
STREAM	STRatospheric Estimation Algorithm from Mainz
SZA	Solar Zenith Angle
TEMIS	Tropospheric Emission Monitoring Internet Service
TENA	Temperate North America
TIR	Thermal Infrared spectral range
TMOD	Tropospheric Chemistry Modelling
TOA	Top-of-atmosphere
TOAR-II	Tropospheric Ozone Assessment Report Phase-II
TROPOMI	Tropospheric Monitoring Instrument (aboard Sentinel-5 Precursor)
ULB	Université Libre de Bruxelles
UPAS	Universal Processor for UV/Vis Atmospheric Sensors
UV-Vis	Ultraviolet and visible spectral range
VOCs	Volatile Organic Compounds
WP	Work Package

2. Evaluation of NO_2 and CO climate data records for ECMWF CAMS

ECMWF's CAMS system assimilates CO from MOPITT and IASI, and NO_2 from OMI (QA4ECV) and GOME-2 (AC-SAF) in their system. Apart from MOPITT CO, these are prototype data products retrieved in a manner consistent with the retrievals done in the ECV Precursor project. ECMWF's experience with these data records is therefore useful to take on board in the development and generation of the data records in this project.

2.1. Status of assimilation of satellite NO_2 in CAMS re-analysis

ECMWF recently tested (Autumn 2022) for the first time the assimilation of TROPOMI NO_2 (from KNMI) along with OMI (KNMI) and GOME-2B/C NO_2 (from AC-SAF) in its IFS system. Adding TROPOMI NO_2 to the assimilation reduces the bias over eastern Asia, where the CAMS system was known to be biased high previously (Figure 2.1 below). The impact of TROPOMI NO_2 assimilation is that it corrects for IFS model issues that led to too much NO_2 in forecast mode over China and the United States. The OMI and TROPOMI NO_2 retrieval approaches are very similar, and the data products agree well, but TROPOMI's spatial resolution and coverage are superior, so that assimilation of TROPOMI NO_2 has a proportionally stronger impact than OMI's.

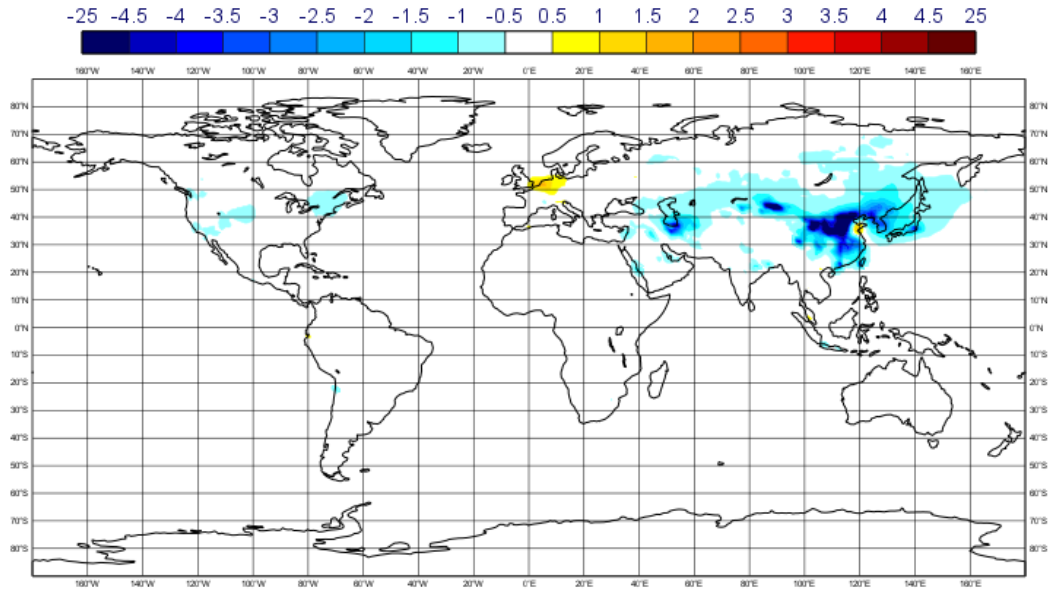


Figure 2-1: Difference in tropospheric NO_2 (ASSIM – CONTROL) when assimilating TROPOMI NO_2 along with OMI and GOME-2 NO_2 in ECMWF's IFS system vs. assimilating only OMI and GOME-2 NO_2.

In a project with KNMI, ECMWF is revisiting its assimilation approach. Instead of the previously used "thinning" approach, ECMWF is now experimenting with so-called 'superobservations'. Superobservations are averaged satellite data representative for the spatial domain of the model grid. An important advantage of superobservations is that they can be accompanied by realistic (gridded) uncertainty estimates that go beyond simple averaged uncertainties. ECMWF indicated that the ECV Precursor data would be more useful to them when filtering

criteria (e.g. solar zenith angle, qa_value, etc.) used in generating the L3 data are included in the data products.

ECMWF prepares taking in QA4ECV NO_2 data from GOME, SCIAMACHY, and OMI for its next CAMS reanalysis (A. Inness, personal communication, 27 May 2024). This is the same data that is used in this project to produce the NO_2 CDR. ECMWF is also testing a new assimilation scheme (4D-Var) in which NO_x emissions (rather than NO_2 columns) are updated based on the satellite NO_2 columns. Preliminary results indicate that the information added by the satellite data persists for a longer time in the assimilated fields, but there are also difficulties still (N. Bousserez, personal communication).

2.2. Status of assimilation of satellite CO in CAMS re-analysis

MOPITT and IASI-B/C CO are routinely assimilated into the CAMS re-analysis system (Inness et al., 2022). Validation revealed that CAMS CO (after assimilation) has a low bias of some 10% against ground based FTIR CO data collected from the NDACC network, and against TROPOMI CO columns. Assimilation of TROPOMI CO columns leads to an improved fit against IAGOS aicraft CO vertical profiles, especially in the lower troposphere. This suggests that IASI and MOPITT CO are not necessarily biased, but rather that the vertical sensitivity of TROPOMI to lower tropospheric CO (retrievals at 2.3 μm) is stronger than the vertical sensitivity of IASI (retrievals at) 4.7 μm which peaks in the middle troposphere. Continuation of IASI CO data in the CAMS system is foreseen, and the differences in vertical sensitivity between IASI and TROPOMI were anticipated and accounted for by application of the observation operator (averaging kernels) in the assimilation procedure.

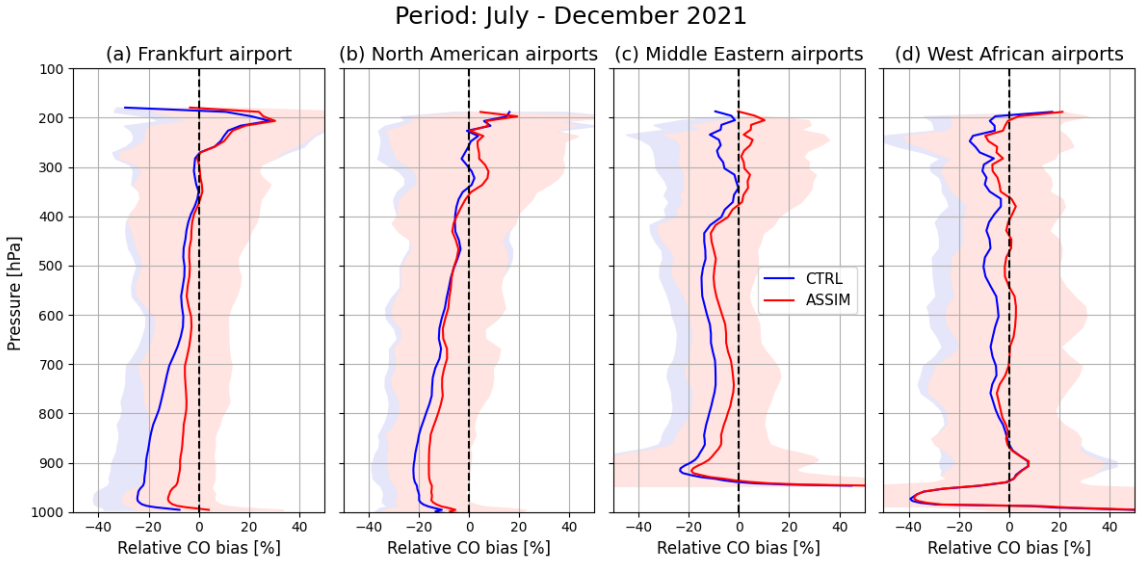


Figure 2-2: Comparison of CAMS CO biases against IAGOS CO profiles observed at various airports around the world. The red curves show the CAMS CO-profiles with the assimilation of TROPOMI CO columns, and the blue curves without the assimilation of TROPOMI CO. From Inness et al. (2022).

ECMWF will continue with the assimilation of IASI CO in its next reanalysis runs and is considering the usage of both nighttime and daytime IASI data. The IASI science team has

advised ECMWF (Antje Inness) to assimilate both daytime and nighttime CO data, since both are of good scientific quality.

2.3. Perspective of assimilation of satellite HCHO in CAMS re-analysis

ECMWF is preparing the assimilation of satellite HCHO data in the IFS system (IFS documentation – Cy48r1, 2023) in the H2020 EU CAMEO-project (https://www.cameo-project.eu/), wherein BIRA (satellite remote sensing of HCHO), KNMI (chemistry in CAMS/IFS), and ECMWF (data assimilation) collaborate.

First technical data assimilation experiments in which CAMS HCHO concentrations were updated via HCHO satellite measurements were not successful. This was anticipated based on the short atmospheric lifetime of HCHO and the lessons learned with data assimilation of NO_2: information added to the system is quickly lost (within hours) after assimilation due to the short atmospheric lifetime of HCHO. The CAMEO-project is now at a stage in which a simplified chemical scheme describing the relationship between isoprene emissions and HCHO concentrations is being defined. With this simple scheme, it will be possible to assimilate (and perform inverse modelling) of satellite HCHO column data to update the isoprene emissions, a more long-lasting impact to the model. A first working version of the data assimilation system that updates isoprene emissions is anticipated by June 2024 (V. Huijnen – personal communication).

One of the lessons learned in working with the satellite data is that negative HCHO columns in the L2 data should not be filtered out when constructing L3 data (A. Inness, personal communication).

3. GEOS-Chem simulations with constraints from HCHO and NO_2 climate data records

3.1. Executive summary

This report investigates the impact of evolving surface emissions in the tropics on tropospheric ozone, using numerical simulations performed over the past decade with the GEOS-Chem chemistry transport model. To ensure the most reliable representation of biomass burning (BB) and anthropogenic sources, tropospheric columns of NO_2 and HCHO derived from ECVs Precursors consortium (satellite products) are used as observational constraints. In addition, tropospheric columns of ozone (TCO) and total columns of CO retrieved from IASI with the SOFRID algorithm serve also for model evaluation on global and regional scales.

The model assessment, based on advanced statistical analyses, reveals that the combination of Global Fire Assimilation System (GFAS) as BB and Copernicus Atmospheric Monitoring Service (CAMS) as anthropogenic emission inventories provides the best overall agreement with the selected satellite observations. Further results indicate that the GEOS-Chem simulation with this couple of emissions captures the annual spatial distributions of NO_2 and HCHO reasonably well compared with OMI retrievals, and that the TCO and CO columns are also in agreement with IASI-SOFRID data. The SOFRID TCO and GEOS-Chem exhibits similar

seasonal variability over the period 2008–2020, but the model produces a positive TCO trend while SOFRID does not provide any significant trend. This modelled trend stems from the increase in anthropogenic emissions of O3 precursors in South and East Asia regions, from the CAMS emission inventory. The difference could be caused by the low sensitivity of IASI to O3 in the boundary layer.

Finally, the ongoing sensitivity simulations with fixed emission scenarii are expected to provide valuable insights into the respective roles of anthropogenic and BB sources in driving the modelled tropospheric column ozone trends, thereby enhancing our under-standing of ozone-climate interactions in tropical regions.

3.2. General objectives and motivation

Tropospheric ozone (O_3) is a harmful pollutant to human health (e.g. Brunekreef and Holgate, 2002; WHO, 2003; Bates, 2005) and control vegetation growth (Ainsworth et al., 2012; Monks et al., 2015). It is also a potent greenhouse gas particularly important in the upper troposphere (e.g. IPCC, 2007; Shindell et al., 2006; Stevenson et al., 2013). Tropospheric O_3 is produced by the photochemical oxidation of volatile organic compounds (VOCs) in the vicinity of nitrogen oxides (NO_x).

The time variation of tropospheric O_3 over the last few decades is characterised by significant regional variabilities. Gaudel et al. (2018) highlighted that tropospheric O_3 is the cause of the main discrepancies between observations and models, particularly in the tropics. Over the last 20 years, ozone precursor emissions have shifted from the mid-latitudes towards the equator (Zhang et al., 2016). In the tropics, anthropogenic emissions are increasing, especially in South-East Asia, and significant changes are expected in Africa as elsewhere.

The overall increase in O_3 in the troposphere therefore comes mainly from the tropics, although the interactions between emissions, transport and chemistry causing this increase remain poorly understood. As part of the Tropospheric Ozone Assessment Report Phase II (TOAR-II) initiative supported by the International Global Atmospheric Chemistry (IGAC), a working group on ozone and its precursors in the tropics has been set up to better understand the increase in tropical tropospheric O_3 (https://igacproject.org/opt-focusworking-group). Ozone and some of its precursors have been observed globally by space-based sensors for several decades. In particular, the tropospheric content of nitrogen dioxide (NO_2) and formaldehyde (HCHO) is documented by UV-Visible spectrometers such as GOME-2 (since 2006), OMI (2005-2021), and more recently TROPOMI (2018-now).

The Laboratoire d'Aerologie (LAERO) is involved in the TOAR-II working group Ozone and Precursors in the Tropics, which aims to determine the origin of the evolution of tropospheric O_3 and its precursors in the Tropics. LAERO is contributing to the ESA CCI+ Precursors project, concerning spaceborne observation of O_3 precursors (HCHO and NO_2) as essential climate variables (ECVs). LAEROs activity is to determine the impact of the evolution of surface emissions in the tropics upon the tropospheric O_3 through numerical simulations of the last decade with the GEOS-Chem chemistry transport model. The surface emission inventories from biomass burning and anthropogenic sources will be constrained using NO_2 and HCHO satellite observations from the ESA CCI+ consortium.

This deliverable presents the use of the L3 ECVs (NO_2 and HCHO) and the L2 data from IASI-SOFRID (O_3 and CO) to constrain GEOS-Chem emission inventories, in order to provide the best simulation to quantify the impact of the evolution of tropical O_3 precursors emissions on the trend of global tropospheric O_3.

The report is structured as follows. Section 3.3 describes the satellite datasets employed. Section 3.4 presents the 3-D GEOS-Chem model (GC) configuration and simulation setup and the strategy of the model assessment. Section 3.5 discusses the main results, including spatial and temporal patterns, as well as comparisons with observations. Finally, Section 3.6 summarizes the conclusions and outlines perspectives for future research.

3.3. Satellite datasets

3.3.1. OMI and TROPOMI satellite observations

The Ozone Monitoring Instrument (OMI), aboard NASA's Aura satellite, is a nadir-viewing imaging spectrometer measuring solar backscattered radiation in the ultraviolet (UV) and visible (VIS) spectral ranges (270–500 nm) with a spectral resolution of 0.42–0.63 nm (Levelt et al., 2006, 2018; Kleipool et al., 2022). It provides daily global coverage through a 2600 km swath, with a nominal nadir pixel size of 13 × 24 km², increased for affected detector rows following the 2007 row anomaly. OMI retrievals of trace gases such as NO_2, O_3, SO_2, and HCHO use the Differential Optical Absorption Spectroscopy (DOAS) technique, with extensive validation against ground-based networks. Its successor, the TROPOspheric Monitoring Instrument (TROPOMI) aboard ESA's Sentinel-5 Precursor (S5P) satellite, extends spectral measurements into the near-infrared (NIR) and shortwave infrared (SWIR) regions, covering 270–2385 nm with a spectral resolution of 0.25–0.5 nm (Veefkind et al., 2012; Ludewig et al., 2020). TROPOMI also provides daily global coverage, with a nadir pixel size of 7 × 3.5 km² improved to 5.5 × 3.5 km² since August 2019 allowing for finer-scale mapping of air pollution and emission sources. Similar to OMI, TROPOMI retrievals are based on DOAS and optimal estimation methods, and are validated using ground-based, airborne, and other satellite observations.

For the model-evaluation, we used the L3-products, which provide in monthly mean gridded of the tropospheric column measurements of NO_2 and HCHO (Essential Climate Variables: ECVs), respectively, which are obtained from the UV–Visible spectrometers OMI, with data products provided by KNMI and BIRA-IASB, respectively.

3.3.2. IASI-SOFRID data

The Infrared Atmospheric Sounding Interferometer (IASI) is a nadir-viewing Fourier transform spectrometer onboard the MetOp-A, MetOp-B and MetOp-C satellites operated by EUMETSAT (Clerbaux et al., 2009). IASI measures the thermal infrared radiation over the spectral range 645-2760 cm^{-1} with an apodized resolution of 0.5 cm^{-1}, providing twice-daily global coverage with a 2° × 2° instantaneous field of view. IASI data are used to retrieve atmospheric composition, temperature, and humidity profiles through radiative transfer inversion schemes. Trace gas retrievals, including CO, O_3, CH_4, HNO_3 and NH_3 rely on their specific thermal infrared signatures. The products are typically delivered as Level 2 datasets containing total columns, vertical profiles, averaging kernels (AKs), and error estimates.

SOFRID-CO retrievals have been validated by in situ airborne data from the IAGOS program (De Wachter et al., 2012; Barret et al., 2025), confirming their reliability for global and regional air quality and climate studies. SOFRID tropospheric O_3 columns have also been validated extensively against in-situ data from O_3-sondes from the WOUDC network (Dufour et al., 2011; Barret et al., 2020).

In this report, we use SOFRID-CO total columns version 2.0 (De Wachter et al., 2012) and SOFRID tropospheric O_3 columns version 3.5 (Barret et al., 2020), in monthly mean gridded to complement the model-evaluation.

3.4. GEOS-Chem model overview, simulation setup and strategy of the model assessment

3.4.1. GEOS-Chem model overview

The GEOS-Chem (GC) is a global three-dimensional (3D) chemical transport model (CTM) that has been used widely in the atmospheric sciences community for studies of atmospheric composition, air quality, climate–chemistry interactions, and long-range transport, and satellite data interpretation (e.g. Bey et al., 2001; Whaley et al., 2015; Eastham et al., 2018; Li et al., 2019; Hammer et al., 2020; Jiang et al., 2022). GC is driven by assimilated meteorological data from NASA's Goddard Earth Observing System (GEOS) of the Global Modelling and Assimilation Office (GMAO). The model simulates the transport, chemical transformation, and deposition of atmospheric trace gases and aerosols.

The meteorological fields used in the GC model are typically taken from GEOS-FP or the Modern-Era Retrospective analysis for Research and Applications, version 2 (MERRA-2) reanalyses, which provide winds, temperature, humidity, surface pressure, and planetary boundary layer height, among other parameters. These datasets ensure that transport processes are consistent with observed atmospheric circulation patterns.

The model operates at various horizontal resolutions (from 4°×5° global to nested regional domains at 0.5°×0.625°) and can represent both tropospheric and stratospheric chemistry. The vertical grid structure of GC follows that of the GEOS meteorological fields. GC model uses 72 hybrid sigma-pressure levels from the surface up to 0.01 hPa, with enhanced resolution in the boundary layer and the upper troposphere-lower stratosphere (UTLS) region. This allows detailed representation of near-surface processes, convective transport, and stratospheric–tropospheric exchange.

The core of GC consists of coupled modules for advection, convection, boundary-layer mixing, gas-phase and heterogeneous chemistry, photolysis, and wet (Liu et al., 2001) and dry (Wesely, 1989) depositions. The chemical mechanisms include detailed treatments of oxidants (HOx, NOx, O_3), carbon compounds, halogens, and secondary aerosol formation (Park et al., 2004; Sherwen et al., 2016).

The emissions compound was configured using the Harvard-NASA Emissions Component (HEMCO) module (Keller et al., 2014; Lin et al., 2021). Emissions inventories incorporated in GC include anthropogenic (ANT), biogenic, biomass-burning (BB), soil, lightning, and volcanic sources, with temporal variations.

3.4.2. Setup of the reference's simulations

We use the parallel version of GC called GEOS-Chem High Performance (GCHP) v14.2.2 (https://geoschem.github.io) to run decadal full-chemistry simulations. All GC simulations are carried out from 2006-01-01 to 2021-12-31 with 72 vertical levels on a 2°x2.5° horizontal grid and use the MERRA-2 reanalysis as the meteorological forcing (Gelaro et al., 2017).

Emissions are the source of chemical species in the atmosphere and are therefore the starting point for modeling air composition. For all simulations, the biogenic VOC emissions will come from the Model of Emissions of Gases and Aerosols from Nature (MEGAN v2.1) inventory (Guenther et al., 2012) and we use default emissions from other natural sources such as lightning (Murray et al., 2012; Sauvage et al., 2007), soil NOx (Hudman et al., 2012), volcanoes. The Tabvle 3-1 describes the couple of inventory emissions for the ANT and BB emissions. The output files contain simulated concentrations on the model grid, sampled at the times corresponding to the overpass of the UV-Vis sounders (OMI and TROPOMI as 13h30 as LT) and the IASI (9h30 as LT). The first two years of all simulation periods is assumed to be a spin-up.

Table 3-1: Characteristics of the GC simulation

Simulations	Couple of emission	Period
REF1	GFAS & CEDS v2	2006 – 2021
REF2	GFAS & CAMS-ANT v6.2	2006 – 2021
REF3	FINN v2.5 & CEDS v2	2006 – 2021
REF4	FINN v2.5 & CAMS-ANT v6.2	2006 – 2021

The first simulation named REF1 uses ANT emissions from the Community Emissions Data System (CEDS v2) (Hoesly et al., 2018) and BB emissions from the Global Fire Assimilation System (GFAS) (Kaiser et al., 2012). REF2 uses GFAS (BB) and the Copernicus Atmospheric Monitoring Service Global Anthropogenic emission (CAMS-ANT v6.2) (Soulie et al., 2024). The REF3 simulation uses the Fire INventory from NCAR (FINN v2.5) (Wiedinmyer et al., 2023) and CEDS. and the REF4 simulation FINN and CAMS.

3.4.3. Strategy of model assessment and choice of the reference simulations

All simulations are systematically evaluated against the latest satellite observations of O_3 precursors and related species. Tropospheric columns of NO_2 and HCHO are retrieved from OMI, while O_3 and CO are retrieved from IASI. NO_2 serves as a key marker of ANT and BB emissions and is directly involved in ozone photochemistry through the NOx-O_3 cycle. HCHO is a major oxidation product of volatile organic compounds (VOCs), making it an important proxy for VOC emissions and photochemical activity. HCHO contributes to the photochemical formation of tropospheric O_3. Although HCHO itself is not a major greenhouse gas, it does contribute indirectly to climate change by reacting in the atmosphere to form compounds that affect the climate.

Unlike the shorter-lived trace gases such as NO_2 and HCHO, CO has a relatively long atmospheric lifetime of approximately 2 to 3 months. This extended lifetime allows CO to be transported over long distances, making it an effective tracer for identifying emission sources at regional to global scales.

O_3 is a secondary pollutant which represents one of the main targets of atmospheric chemistry modelling to simulate and forecast regional air quality. O_3 and NO_2 are gathered in the Ox family as key air quality species because of their oxidation capacity which makes them harmful for human health.

By jointly analysing these species, the evaluation provides a robust constraint on the GC's representation of emissions, chemistry, and transport processes, and helps identify the most consistent emission configuration to better constrain the emissions inventories.

To assess the performance of the GC simulations, we selected several regions across the globe as represented in the Figure 3-1. Namely, these regions include four oceanic zones, which are used as reference areas with negligible emissions, and a range of continental regions that are representative of either significant ANT NO_2 emissions or major BB emissions.

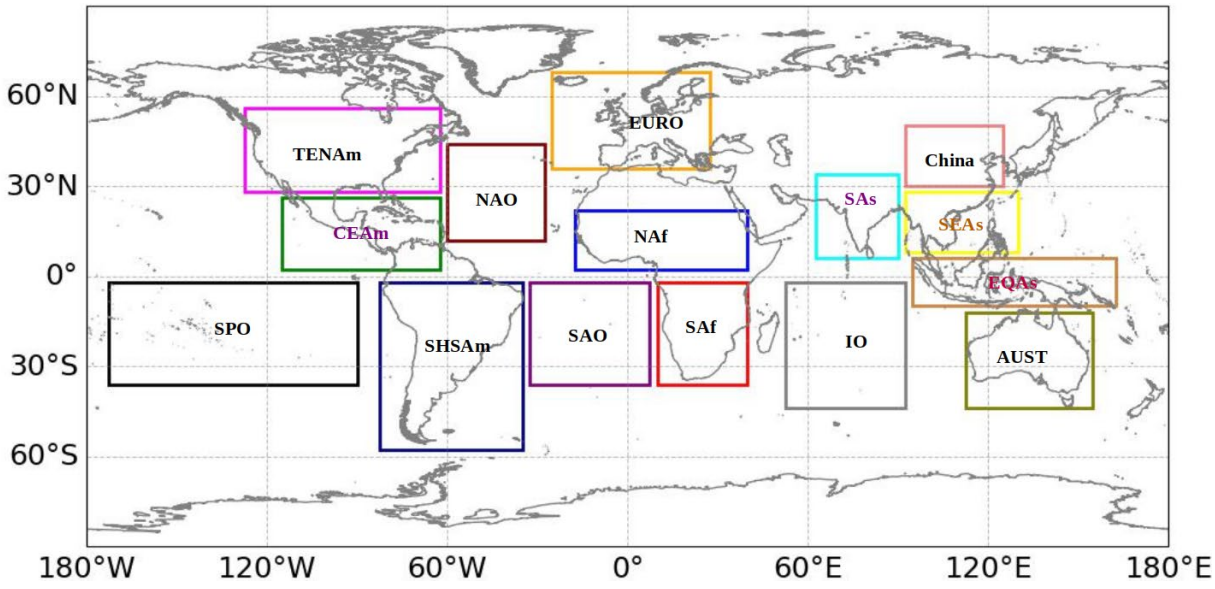


Figure 3-1: Subdomains for the different regions of the model output analysis

We also applied the mask defining oceanic (mask value: 0) and continental (mask value: 1) regions provided in the ECVs data ("land_water_mask") to all regions in the GC simulations (Table 3-2), allowing to extract values specifically from continents and/or oceans for a more accurate comparison between the simulations and observations.

Table 3-2: Abbreviations and corresponding regions depicted in Figure 3-1.

Regions	Description	mask
TENAm	Temperate North America	1
CEAm	Central America	1
SHSAm	Southern hemisphere south America	1
EURO	Europe	1
NAf	Northern Africa	1

SAf	Southern Africa	1
SEAs	Southeast Asia	1
SAs	South Asia	1
China	Specific urban area in China	1
EQAs	Equatorial Asia	1
AUST	selected region in Australia	1
SPO	South Pacific Ocean	0
SAO	South Atlantic Ocean	0
NAO	North Atlantic Ocean	0
IO	Indian Ocean	0

We finally performed statistical analyses of the model versus observations comparisons (Biases and Taylor Diagrams) for the four key species (NO_2, HCHO, O_3 and CO) based on their global and regional monthly mean concentrations (Figure 3-1).

We firstly calculate the mean bias error (MBE) which is defined as the difference between the columns of the chemical species (NO_2, HCHO, CO and O_3) derived from the GC model and those obtained from satellite observations (OMI/IASI). To complement the bias statistical analysis, we use Taylor diagrams in order to evaluate the variabilities of the columns from the different GC simulations relative to the satellite's products (OMI/IASI). The Taylor diagrams help us to select the couple of emission inventories (ANT and BB inventories emissions) that best matches the observed distributions.

The Taylor diagram simultaneously displays the three following statistical metrics:

- **Correlation coefficient (R):** quantifies how well the model captures the spatial or temporal patterns of the observed data. The R-values range from 0 (no correlation) to 1 (perfect correlation), and are represented by the azimuthal angle in the diagram.
- **Standard deviation (std) ratio:** represents the variability of the model compared to the observations. It is depicted as the radial distance from the origin. A ratio below 1 suggests the model underestimates the variability; a ratio above 1 indicates an overestimation of the variability.
- **Centered Root Mean Square Error (RMSE) ratio:** quantifies the precision of the model relative to the observations, excluding any systematic bias. It is shown as the distance between the model point and the reference point (observations).

3.5. Results and interpretations

3.5.1. Assessment of the GEOS-Chem simulations with the satellite data

This section examines the comparison of the NO_2 and HCHO tropospheric columns from GC simulations with the OMI observations, as well as the tropospheric ozone columns (TOC) and the CO total columns from IASI and the GC for the 2008–2020 period. The evaluation of GC simulations against satellite observations is performed on tropospheric columns (NO_2, HCHO and O_3) and total columns (CO), without application of the AKs matrix to the model columns. Due to the short atmospheric lifetimes of NO_2 and HCHO species, their concentrations are largely confined to the lower troposphere. We acknowledge the fact that by not taking into

account the impact of the vertical sensitivity of satellite measurements, a bias can be introduced in the comparison with GC simulations. This bias will be small when GC and TM5 simulations compare reasonably well. Finally, it is important to note that in the model-evaluation, we use the simulated concentrations on the model grid, sampled at the times corresponding to the overpass of the UV-Vis sounders (OMI as 13h30 as LT) and the IASI (9h30 as LT). This allows us to choose the best inventory of ANT emissions and BB to best reproduce satellite observations with the models.

3.5.2. Bias analysis

The OMI data provides the best coverage before 2020, and SOFRID O_3 and CO column data are available for the 2008–2020 period. At this stage, we have not included the tropospheric columns from TROPOMI in the analysis as model-evaluation requires multi-year satellite data to capture variability and represent both seasonal cycles and long-term trends. The following Figures 3-2 and 3-3 displays biases for the global and regional domains from Figure 3-1 and Table 3-1.

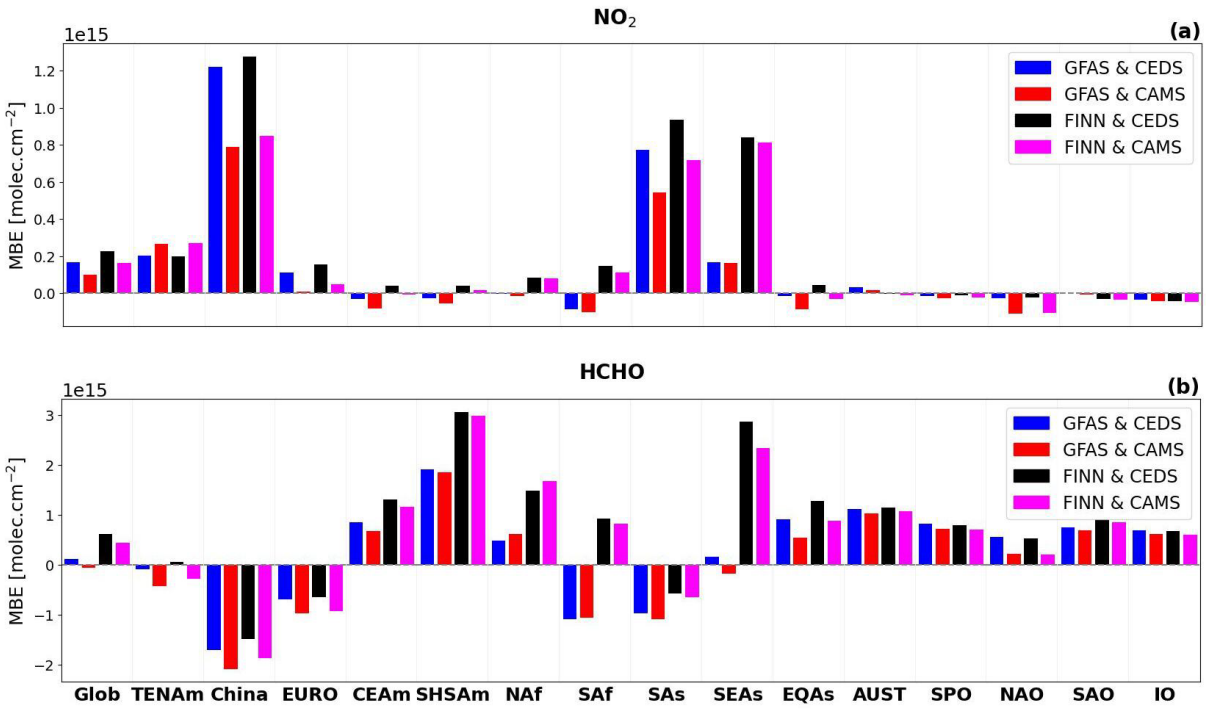


Figure 3-2: MBE for the GC relative to OMI tropospheric column, *over the 2008–2020 period* for the global and the regional domains (a) NO_2 and (b) HCHO (blue) REF1, (red) REF2, (black) REF3 (magenta) REF4.

NO_2 is emitted both by ANT and BB sources. In Figure 3-2 (a), the blue and black curves represent results using the CEDS ANT emission inventory, while the red and magenta curves correspond to simulations using CAMS ANT emissions. Figure 3-2 (a) shows that CAMS and CEDS produce similar biases for both global and oceanic regions. For both inventories, the largest biases are located over Asian regions with the largest ANT emissions: China, SAs, and SEAs. The other important NO_2 emitters, Europe and TENAm are characterised by much lower

biases meaning that the inventories better represent their emissions than those of Asian regions.

Over China and SAs the biases from the simulations with the CEDS inventory (REF1 and REF3) are significantly larger than those from simulations with the CAMS inventory (REF2 and REF4). The differences may stem from their methodology, spatial resolution, and data sources. The CEDS provides a long-term global emission record using generic proxies (e.g. population density, land use, etc.), which may not capture local hotspots and/or seasonal variations (e.g., McDuffie et al., 2020; Chen et al., 2025), whereas CAMS incorporates observations and region-specific data with higher spatial and temporal resolution, offering more accurate emissions in complex regions such as China and SAs. For the other regions, the differences between simulations with both ANT inventories concerning NO_2 are not significant.

Concerning BB emissions, the use of GFAS (blue REF1/red REF2) provides a slightly lower NO_2 biases in regions with intense BB activity (NAf and SAf) relative to FINN (black REF3/magenta REF4). The GFAS inventory therefore provides better emissions of NO_2 emissions over Africa than FINN. This result is in agreement with Wiedinmyer et al. (2023) who have shown that the use of FINN v2.5 tends to an overestimation of tropospheric NO_2 columns compared to other BB emission inventories in certain regions (e.g. SEAs, NAf, SAf). Biomass burning emission inventories differ due to methodological approaches. FINN uses satellite-detected active fires (MODIS hotspots) and fixed emission factors by vegetation type and fuel load at 1 km resolution, which can overestimate emissions by counting many small fires, especially in regions with widespread low-intensity burning (Wiedinmyer et al., 2011, 2023). However, GFAS uses Fire Radiative Power (FRP) from MODIS and scales emissions by fire intensity at 0.5° × 0.5° resolution, producing lower totals and better capturing peatland fires that burn beneath the canopy and may be missed by hotspot-based inventories (Kaiser et al., 2012).

For HCHO (Figure 3-2 (b)), the use of GFAS generally results in lower biases with OMI than the use of FINN, in regions with intense BB emissions such as SHSAm, NAf and EQAs. GFAS also provides slightly weaker biases over oceanic regions such as SPO, NAO, SAO and IO. For the whole globe, the use of CAMS results in an almost null bias while FINN provides a significant positive bias.

The comparison between CO distributions from simulations with the CAMS and CEDS ANT emission inventories, (Figure 3-3 (a), blue/black for CEDS vs. red/magenta for CAMS), does not reveal significant differences for the biases across all regions (oceanic, regional, and global) throughout the analysed period (*2008–2020*). The use of CAMS or CEDS has therefore a limited impact on modelled CO columns.

More significant discrepancies arise when comparing GFAS and FINN BB emission inventories, which exert a stronger impact on CO distributions, especially in BB intense regions. The results clearly indicate that the use of GFAS leads to a systematic underestimation of the CO columns except over Asian regions and SHSAm SAf, biases from simulations with the FINN inventory are very low.

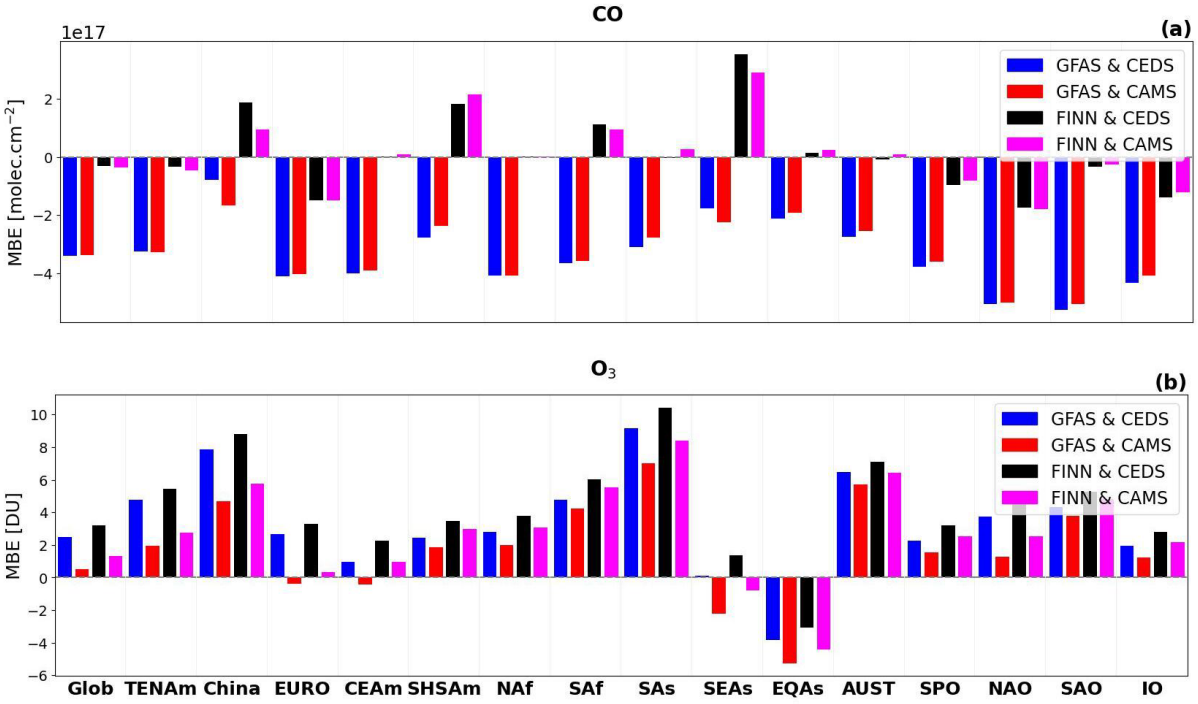


Figure 3-3: MBE for the GC relative to IASI column, *over the 2008–2020 period* for the global and the regional domains (a) total column of CO and (b) tropospheric ozone column (blue) REF1, (red) REF2, (black) REF3 (magenta) REF4

Figure 3-3 (b) presents the distribution of the bias in the TOC (GC-IASI). Using the CEDS emission inventory (blue/black) leads to slightly lower overestimations than using CAMS (red/magenta) across all regions. Therefore, the analysis of the biases only is not sufficient to determine which emission inventory allows a more accurate representation of TOC.

To make the right choice of inventories, it is crucial to address the ability of the simulations to represent the spatiotemporal variations of the different target species.

3.5.3. Taylor Diagram analysis

In this section, we present and discuss the Taylor diagrams of the observations/simulation's comparisons. Figures 3-4 (a) and 3-4 (b) display, the results for NO_2 and HCHO respectively. The blue, red, black, and magenta colors represent the REF1, REF2, REF3, and REF4 simulations, respectively, for the global and regional domains from Figure 3-1 and Table 3-1.

For NO_2, the variability with FINN as BB inventory (black/magenta colors in Figure 3-4 (a)) is largely overestimated, with standard deviation ratios larger than 1, particularly in regions impacted by BB such as SAs, EQAs, CEAm, NAf, SAf, SEAs (standard deviation ratios > 4.0) and SHSAm where the ratios range from 1.5 to 4.0.

The correlation coefficients (R-values) from FINN simulations are generally much lower than those obtained using the GFAS inventory, especially over some regions impacted by BB such as EQAs, NAf, SHSAm, CEAm, SAs and SEAs (R-values around 0.2). GFAS is therefore more able to reproduce the NO_2 columns variations resulting from BB in both amplitude (standard deviation ratios) and phase (R-coefficient).

For HCHO (Figure 3-4 (b)), the simulations using GFAS generally exhibit higher correlation coefficients and standard deviation ratios closer to the reference point compared to those using FINN. In major BB regions such as SHSAm, GFAS yields R-values around 0.8 with a standard deviation ratio close to 1, while FINN gives lower correlations (R ≈ 0.6) and higher variability (std. dev. ratio > 1), indicating an overestimation of the amplitude of the variability relative to OMI observations. At the global scale, GFAS simulations remain better correlated (R ≈ 0.6) with variability close to the reference, whereas FINN simulations show much lower correlation coefficients (R ≈ 0.2) and too large variability.

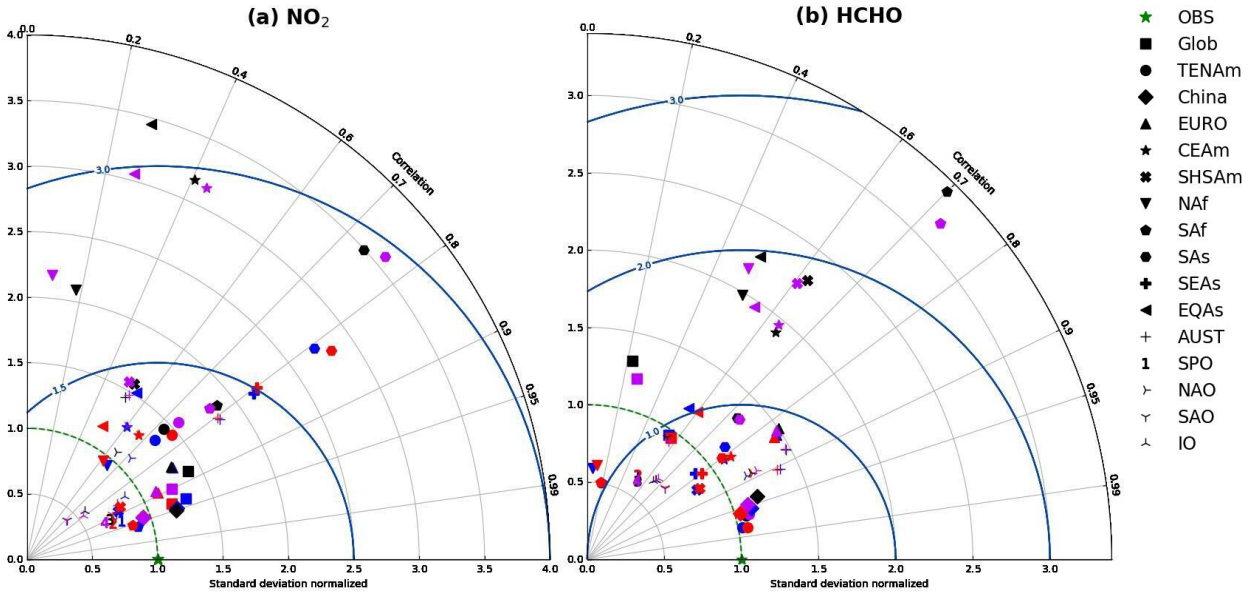


Figure 3-4: Taylor diagrams for (a) NO_2 and (b) HCHO tropospheric columns over the 2008–2020 period. Each point corresponds to a different simulation, identified by color and symbol. The reference observation is positioned at a normalized standard deviation of 1 and a correlation coefficient of 1. The distance from this reference point reflects the centered RMSE, with simulations located closer to it representing better overall performance.

The overall analysis (MBE and Taylor diagram) indicates that the GFAS and CAMS emission inventories provide the best consistency with NO_2 observations from OMI. For HCHO, GFAS performs better than FINN, showing better variabilities and lower biases.

Figure 3-5 summarizes the overall performance of the GC simulations for the total column of CO and TOC over the 2008–2020 period, based on comparisons with IASI-SOFRID products.

Figure 3-5 (a) shows that simulations using FINN (black/magenta) as BB emissions exhibit too large CO variabilities with ratios from 1.2 to ~3.5. It is noteworthy that the combinations FINN/CEDS leads to the largest ratios meaning much too high variabilities relative. Simulations with GFAS (blue/red) provides in better agreement with the observations with standard deviation ratios between 0.5 and 1.5. In addition, GFAS-based simulations generally display higher correlation coefficients ratio (R-values) at both global and regional scales (e.g., CEAm, EURO, TENAm) and result in lower centered RMSE ratios than FINN. These results indicate that GFAS emission inventories provides a better representation of BB emissions than FINN.

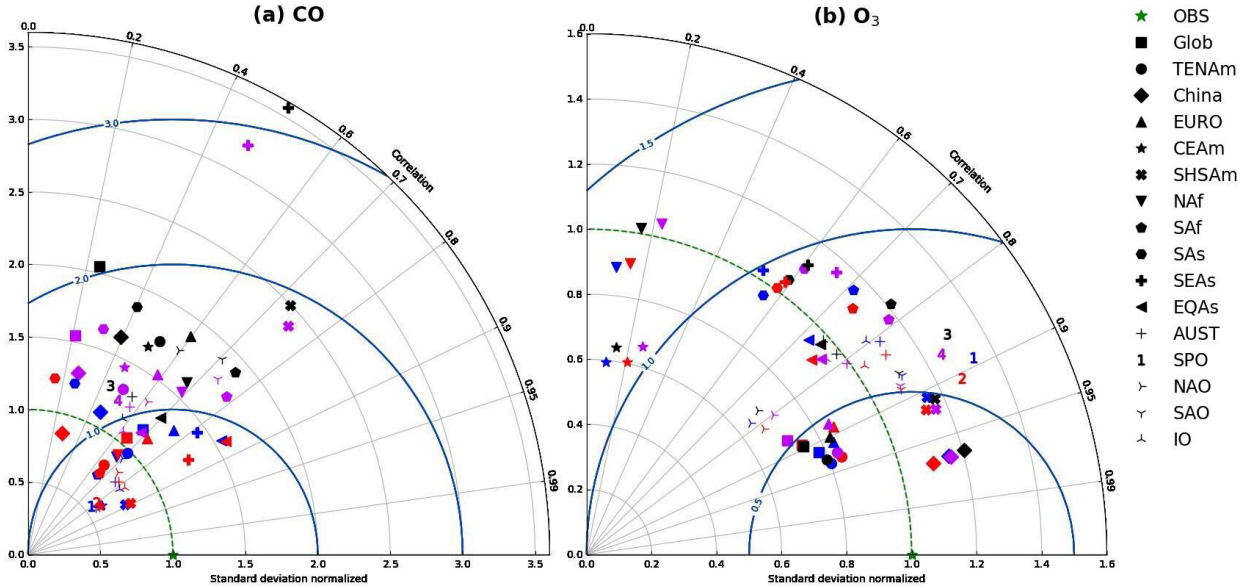


Figure 3-5: ***Taylor diagram for (a) total column of CO and (b) tropospheric O_3 column over the 2008–2020 period***

We present in the figure 3-5 (b) the Taylor diagram for TOC comparisons between the GC simulations and the SOFRID products. It clearly shows that all the GC-simulations are clustered between ocean regions, regions with high ANT emissions, and regions with high BB emissions. The weakest correlations with IASI-observations are found in the NAf and CEAm regions. However, R-values exceed 0.55 for all GC simulations over all regions, with standard deviation ratios ranging from 0.5 to 1.3. The agreement between GC and the SOFRID TOC is therefore good but the lack of differences between simulations show that TOC is not a good target for emission inventories selection.

Our results indicate that CAMS is the best ANT emission inventory based on the ability of the simulations to reproduce NO_2 biases and variabilities. Based mostly on the analysis of the variabilities of the target species we can also conclude that GFAS offers the most consistent representation of BB emissions. The CAMS–GFAS simulation (REF2) shows the best overall agreement with the satellite products.

3.5.4. Global distributions of ozone and its precursors

Figures 3-6 and 3-7 display a comparison of the 2008-2020 annual averages between satellite retrievals (OMI and IASI) and model simulation. According to the previous section, we selected the “best” (REF2) simulation using a combination of CAMS ANT and GFAS BB.

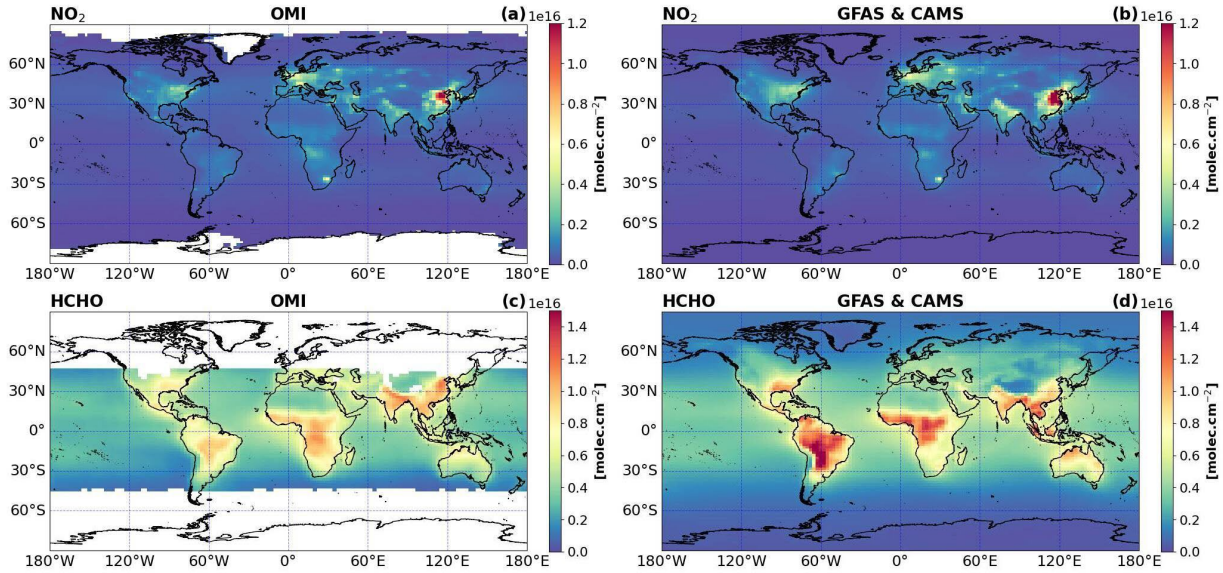


Figure 3-6: Tropospheric NO_2 column from OMI (a) vs GC (b) and HCHO tropospheric columns retrieved from OMI (c) and the that simulated by GC (d) on the 2008-2020 period.

The distributions of tropospheric NO_2 columns from OMI are largely consistent with the GC simulation and (Figures 3-6 (a) and (b)) and the model captures very well the overall spatial distribution and the emission hotspots. However, the model tends to overestimate tropospheric NO_2 over regions that are heavily industrialised and densely populated, such as China, TENAm, SAs and EURO. This discrepancy can be explained by sampling biases in satellite NO_2, which tend to underestimate tropospheric column values (e.g., Geddes et al., 2012; Boersma et al., 2016).

Concerning the HCHO tropospheric columns, the OMI and GC columns display similar features (Figure 3-6 (c) and (d)) with a similar order of magnitude (1E+16 molec.cm^{-2}). The maxima, related to large biogenic (e.g. isoprene) emissions (e.g. Guenther et al., 2006, 2012, Lathière et al., 2006) are located over the same regions (e.g. Indochina peninsula, SHSAm, NAf). For OMI, the North Hemisphere latitudes above 40°N and the South Hemisphere latitudes above 40°S are lacking (due to snow and ice coverage) which is not allowing to make a complete comparison.

The influence of BB emissions on HCHO is clearly overestimated by GC, particularly in the SHSAm, NAf and SAf regions. In these areas, GC tends to overestimate HCHO columns, reflecting uncertainties in the GFAS BB emission inventories. Additionally, the chemical conversion of non-methane volatile organic compounds (NMVOCs) and isoprene to HCHO can produce excess concentrations if oxidation or loss processes are oversimplified. Further discrepancies may arise from limitations in the model's representation of transport and deposition processes (e.g. Hoque et al., 2024, Wang et al., 2025).

Figure 3-7 (a) and (b) show that the general pattern of the CO annual distributions form SOFRID is correctly reproduced by the REF2 simulation (Figure 3-7). Nevertheless, GC clearly underestimates the CO total columns globally in agreement with what has been previously shown in the evaluation of the simulations. These results are not unexpected and have already been reported in studies using GC-model especially in the Northern Hemisphere, which may

be due to an overestimation of OH or missing CO emissions (e.g., Lin et al., 2024; Kopacz et al., 2010, Kim et al., 2022).

The distributions of TOC from the REF2 simulation agrees well with the SOFRID retrievals (Figure 3.7 (c) and (d)). However, it displays bands of overestimated TOC at the tropical outer boundaries (30°S and 30°N). This discrepancy is unlikely to reflect excessive stratospheric influence, as GC calculates TOC using MERRA-2 meteorology and a dynamically defined tropopause. Instead, this discrepancy is likely derived from methodological differences in TOC definition and vertical sensitivity: SOFRID derives TOC from vertically smoothed O_3 retrievals, constrained by a priori climatological profiles linked to the WMO tropopause, while GC integrates O_3 up to a dynamic tropopause defined by the model.

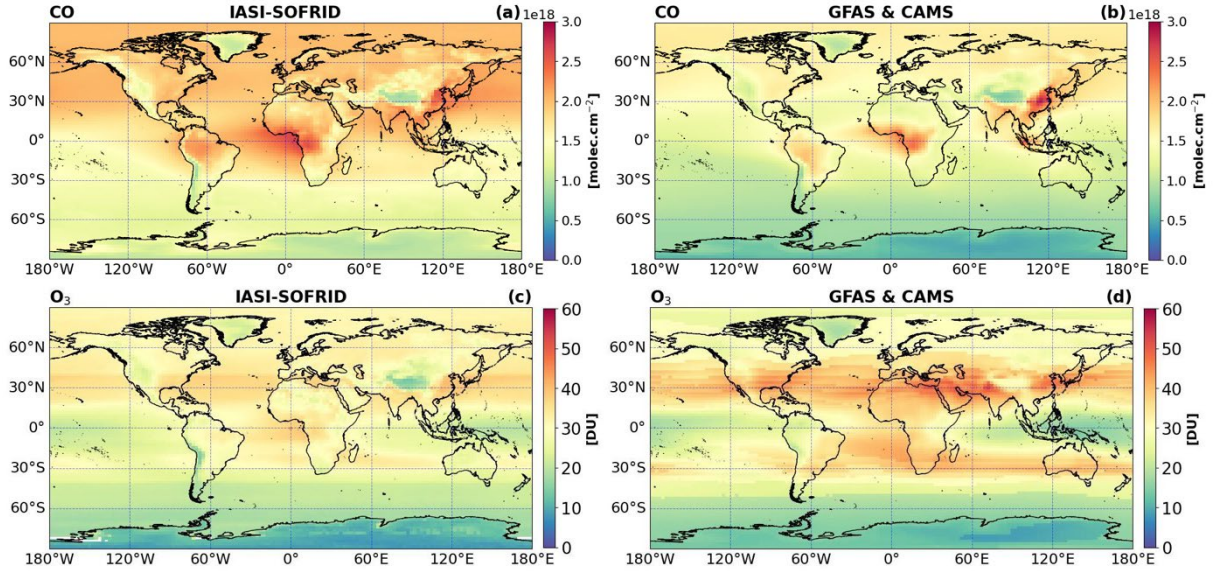


Figure 3-7: Yearly distributions of CO total columns (molecule.cm^{-2}) from (a) SOFRID (b) GC and TOC (DU) from (c) SOFRID (d) GC averaged over the 2008-2020 period

In the following section, we present and discuss the TOC trends derived from SOFRID and from the GC REF2 simulation.

3.5.5. Global ozone trends over 2008 -2020 period

The raw datasets from SOFRID and the GC contain noise. The TOC ozone trend is also affected by seasonal cycles and interannual variabilities such as the El Niño-Southern Oscillation (ENSO), making it difficult to clearly detect a long-term evolution of the TOC. To overcome this difficulty, we applied the following simplified model which have already been used by Wespes et al. (2016) to SOFRID and GC TOC monthly time series for the 2008–2020 period:

$$O_3(t) = C + A_1 \cdot \cos\left(\frac{2\pi\,(t-\varphi 1)}{12}\right) + \frac{mt}{12} + A_2 \cdot \cos\left(\frac{2\pi\,(t-\varphi 2)}{24}\right) + A_3 \cos\left(\frac{2\pi\,(t-\varphi 3)}{6}\right) + \alpha \cdot ONI(t) \quad \text{(eq. 1)}$$

Where:

t: months

C: monthly TOC

$A_1 . \cos\left(\frac{2\pi\,(t-\varphi 1)}{12}\right)$: **annual seasonal cycle (**12 months period)

$A_2 . \cos\left(\frac{2\pi\,(t-\varphi 2)}{24}\right)$: **semi-annual variability cycle (**24 months period)

$A_3 . \cos\left(\frac{2\pi\,(t-\varphi 3)}{6}\right)$: **biannual variation (**6-months period)

$\frac{mt}{12}$: annual linear trend

$\varphi 1, \varphi 2 \text{ and } \varphi 3$: phase shifts of the respective cosine terms

α. ONI (t): sensitivity to the ENSO events. The Oceanic Niño Index (ONI) data were obtained from the NOAA/Physical Sciences Laboratory.

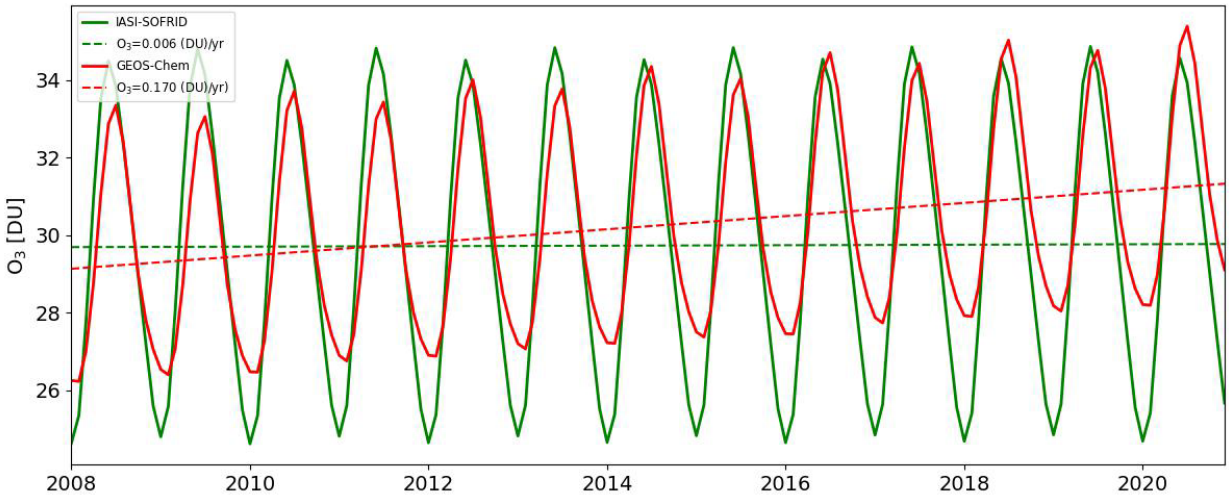


Figure 3-8: Time series of the TOC between 2008 and 2020, as derived from SOFRID (green color) and GC (red color). The dashed lines correspond to the linear trends derived from the simplified model (equation 1).

TOC from SOFRID and GC (Figure 3-8) display similar seasonal variability over the 2008–2020 period, but the model produces a positive trend of +0.170 DU/yr when SOFRID provides no significant trend (+0.006 DU/yr). This difference is consistent with rising ANT emissions of O_3 precursors in South and East Asia (e.g., Bowman et al., 2022), accounted for in the GC emission inventories.

The IASI instrument, operating in the thermal infrared is more sensitive to ozone concentrations in the mid-and upper troposphere and less near the surface where most of the TOC increase related to ANT activities occurs. A study from the TOAR-I project has shown important discrepancies UV-Vis and TIR sensors for the TOC trends (Gaudel et al. 2018). TOC retrieved from UV-Vis sensors provided positive global trends while retrievals from TIR sensors resulted in negative (FORLI algorithm) or insignificant trends (SOFRID). Comparing three IASI retrievals Pope et al. (2024) confirm the absence of significant TOC trends with this sensor such as shown with SOFRID in Gaudel et al. (2018). The reason from the discrepancy between UV-Vis and TIR sensors was not understood at the time of Gaudel et al. (2018) but some possible causes maybe disclosed by the latest assessment study of satellite TOC from the TOAR-II project.

3.5.6. Conclusion and perspectives

We have performed four long-term (2006–2021) full-chemistry simulations with the 3D CTM GEOS-Chem model using the MERRA-2 as meteorological forcings to evaluate and constrain emission inventories. The GFAS and FINN v2.5 inventories for BB emissions inventories and the CAMS-ANT v6.2 and CEDS v2 for ANT emissions were evaluated against OMI ECVs for O_3 precursors (NO_2 and HCHO) and against SOFRID IASI retrievals for O_3 and CO columns. From this model evaluation we concluded that the combination of GFAS for BB and CAMS for ANT emission provides the best overall agreement with the selected satellite observations.

GFAS clearly improves the representation of the variabilities of HCHO and CO columns compared to FINN which largely overestimates these variabilities. The use of CAMS allows reducing the positive biases of NO_2 columns over highly polluted Asian regions compared to CEDS.

The GC simulation reproduces the annual spatial distributions of NO_2 and HCHO reasonably well compared to OMI retrievals. Low data coverage does not allow to conclude about the simulated HCHO distributions at latitudes higher than 40°. Tropospheric ozone column and CO columns are also consistent with IASI-SOFRID. Significant TOC overestimations are found around 30°S and 30°N, likely linked to overestimated stratospheric influence.

The" best" set of inventories has now been selected. We will proceed to perform sensitivity simulations to document the impact of emissions on the evolution of the TOC. The first sensitivity simulation has been performed setting the ANT emissions constant to the 2006-2008 average in the tropics. The second one is similar with fixed BB emissions. Comparisons between these sensitivity simulations with the REF2 simulation will enable to determine the impact of the evolution of the two different types of emissions on the TOC trend.

4. Assessment of the variability and trends of HCHO columns over Africa

4.1. Executive summary

This report presents an assessment of the variability and trends of tropospheric formaldehyde (HCHO) columns over Africa based on long-term satellite observations from OMI CCI+ and simulations performed with the regional chemistry-transport model MAGRITTE over 2005-2018. The objective is to evaluate the capacity of the model to reproduce observed HCHO distributions and trends, and to interpret these in terms of changes in emissions, land cover and climate.

Overall, we find that the model successfully captures the main spatial and seasonal variability of HCHO across the continent and exhibits high correlations with OMI data. Observations indicate widespread positive HCHO trends across Africa between 2005 and 2018, ranging from +0.4 to +1 %yr^{-1}, with the strongest values in southern African regions. MAGRITTE succeeds in reproducing the trend patterns but underestimates their magnitude. Systematic biases remain in average HCHO columns, with overestimations in equatorial forests and underestimations in southern Africa, likely reflecting uncertainties in isoprene emission factors and vegetation types. Methane oxidation is found to be the dominant source of HCHO (50-60% of total columns), except over tropical forests where biogenic emissions prevail.

Biogenic emission trends, while having only a modest overall impact, improve the agreement between model and observations. Increasing anthropogenic activity and declining biomass burning contribute to the observed regional contrasts. Sensitivity tests highlight the crucial role of soil NO emissions in driving regional HCHO trends through their influence on OH concentrations. Large discrepancies between existing soil NO inventories introduce significant uncertainties in the simulated trends, underscoring the strong coupling between NO_X, OH and VOC oxidation processes and the importance of accurately representing natural emission sources.

This work demonstrates the complementarity of long-term satellite datasets and regional chemistry-transport modelling for quantifying changes in atmospheric composition due to climate, and to changes in emissions and land use over Africa. Future work will extend the analysis to more recent years and explore joint use of HCHO and NO_2 CCI+ data within the ESA PIRAMID project framework.

4.2. Introduction

Emissions of non-methane volatile organic compounds (NMVOCs) play a crucial role in air quality and climate. They act as precursors of secondary organic aerosols (SOAs; Claeys et al., 2004; Hallquist et al., 2009) and influence tropospheric ozone concentrations through interactions with nitrogen oxides (NOX) (Atkinson, 2000; Ryerson et al., 2001; Saunier et al., 2020). On the global scale, biogenic sources dominate NMVOC emissions, accounting for about 85%, compared to 12% from anthropogenic and 3% from pyrogenic sources (Granier et al., 2019; Stavrakou et al., 2018). Among the biogenic volatile organic compounds (BVOCs), isoprene (C5H8) is by far the most dominant BVOC emitted by vegetation, representing about half of global NMVOC emissions (Guenther et al., 2012; Sindelarova et al., 2014).

Formaldehyde is a key product of VOC oxidation and can be reliably detected by both ground- and space-based instruments. While direct emissions contribute only marginally, the oxidation of methane (CH4) accounts for about 60% of the global HCHO budget (Stavrakou et al., 2009). Because of its long lifetime, this contribution acts as a background source. In contrast, short-lived volatile organic compounds (VOCs) such as isoprene and monoterpenes exert a stronger influence on the spatial variability of HCHO. Formaldehyde is also relatively quickly removed via photolysis and reaction with hydroxyl radical (OH), with a typical lifetime of approximately 5 h (Stavrakou et al., 2015). Importantly, VOCs-NOX interaction affects OH concentrations, thereby modifying both their lifetimes and degradation pathways. Due to its short lifetime and rapid chemical processing, transport processes play a limited role in shaping the observed HCHO distribution except under certain conditions such as nighttime, winter, or low NOX environments (Marais et al., 2012). Consequently, HCHO is an excellent tracer, and its observed abundancies can directly be linked to the emissions of reactive NMVOCs.

In recent years, air pollution in Africa has become a growing concern, driven by rapid population and economic development, with serious environmental and health implications (Brauer et al., 2012; Mead et al., 2023; Petkova et al., 2013; Singh et al., 2020). Major contributors to deteriorating air quality include emissions from megacities such as Lagos and Kinshasa, oil exploitation (e.g. in Nigeria), coal mining and power generation in South Africa, widespread biomass burning, as well as aerosol dust predominantly from the Sahara and Sahel are key examples of sources affecting air quality over the continent. Glob-ally, anthropogenic

activities are the dominant source of NOX (Soulie et al., 2024). Howev-er, natural processes, particularly soil and lightning emissions, account for roughly 30 % of the total global NOX budget and play an even larger role in remote regions (Jaeglé et al., 2005). In Africa, NOX release from soils, due to soil microbial activity and fertilizer use, can be strong enough to be detected by satellites (Jaeglé et al., 2004, 2005; Stavrakou et al., 2013), with important consequences for atmospheric OH concentrations. In addition, ev-ergreen tropical forests across western and equatorial Africa represent major sources of isoprene (Guenther et al., 2012; Lathière et al., 2006; Messina et al., 2016; Sindelarova et al., 2022). Current estimates suggest that about 80 % of total isoprene emissions originate in tropical regions, reflecting the combination of high temperatures, intense solar radia-tion and the widespread distribution of broadleaved trees (Guenther et al., 2012; Opacka et al., 2021).

The Tropospheric Chemistry Modelling (TMOD) team at the Royal Belgian Institute for Space Aeronomy (BIRA-IASB), partner of the ESA CCI+ Precursors project, aims to improve the understanding of the processes driving the observed variability of the Ozone Monitor-ing Instrument (OMI) CCI+ HCHO column densities over Africa. This is achieved through multiyear numerical simulations using the MAGRITTE CTM. Satellite ECV HCHO from the ESA CCI+ consortium will be used as benchmark for model evaluation and validation.

This report is structured as follows. Section 4.3 describes the satellite datasets employed. Section 4.4 presents the regional CTM MAGRITTE configuration and simulation setup. Section 4.5 discusses the main results, including spatial and temporal patterns. Finally, Section 4.6 summarises the conclusions and outlines perspectives for future research.

4.3. Satellite OMI formaldehyde observations

Aboard NASA AURA spacecraft launched in 2004 (Levelt et al., 2006), OMI is a nadir-viewing imaging spectrometer observing Earth's global solar backscatter radiation in the ultraviolet–visible spectral window at a spectral resolution of about 0.5 nm. It has an ear-ly afternoon overpass time (13:30 LT) and provides daily global observation at a spatial resolution of 13 × 24 km² at nadir, increased to 13 × 48 km² for affected detector rows following the 2007 row anomaly. Here we use tropospheric OMI CCI+ HCHO L2 columns at that were developed in the framework of the ESA CCI+ consortium by BIRA-IASB (De Smedt, 2025). The retrieval of trace gases such as NO_2, O_3, SO_2, and HCHO uses the Differential Optical Absorption Spectroscopy (DOAS) technique, with extensive validation against ground-based networks.

4.4. MAGRITTE model and simulation setup

4.4.1. MAGRITTE CTM

Simulations of atmospheric composition are performed using a CTM, MAGRITTEv1.1 (Müller et al., 2019), which is based on the global CTM IMAGES (Bauwens et al., 2016; Müller and Brasseur, 1995; Stavrakou et al., 2015). The model simulates the transport, chemical transformation, and deposition of atmospheric trace gases and aerosols in the troposphere. It computes the concentrations of 170 chemical species with a 6-hour time step and a 6-month spin-up time. First, MAGRITTE is run in its global configuration at a spatial resolution of 2° × 2.5° (latitude, longitude). The global simulation provides the boundary conditions for the regional configuration of MAGRITTEv1.1, which operates at the finer horizontal resolution of

0.5° × 0.5° from the surface up to the lower stratosphere, using 40 hybrid sigma-pressure vertical levels.

MAGRITTE offers a state-of-the-art representation of VOC oxidation chemistry, especially in low NO_X conditions. The oxidation mechanism of isoprene in MAGRITTE builds on the Leuven Isoprene Mechanism (Peeters et al., 2014), the Caltech mechanism (Wennberg et al., 2018), and the laboratory data of Berndt et al. (2019). A detailed description of the model is provided by Müller et al. (2019). Regarding the influence of isoprene on NO_X, MAGRITTE accounts for organic nitrate formation via isoprene oxidation by OH and NO_3 (Kwan et al., 2012; Paulot et al., 2009; Wennberg et al., 2018), NO_X-recycling pathways such as photolysis (Müller et al., 2014), and NO_X terminal sinks through heterogeneous hydrolysis in aqueous aerosols (Romer et al., 2016) and dry deposition (Nguyen et al., 2015).

4.4.2. Model setup and simulations

Simulations of monthly HCHO tropospheric columns at a 0.5° resolution are performed with MAGRITTEv1.1 model over the African domain delimited by 30°S-17°N and 18°W-56°E (Figure 4-1) from 2005 to 2018. The output files contain simulated HCHO concentrations on the model grid, sampled at the overpass of the OMI sounder, i.e., at 13:30 LT.

The meteorological fields used in MAGRITTE are provided by the European Centre of Medium-range Weather Forecasts Reanalysis v.5 (ERA5) global reanalyses (Hersbach et al. (2020). The standard simulation accounts for all the VOC sources prescribed as follows. The model uses anthropogenic emissions of NO_X, CO, SO_2, NH_3, and non-methane VOC species from the global CAMS-GLOB-ANTv5.3 inventory (Granier et al., 2019). The biomass burning inventory is provided by the Quick Fire Emissions Dataset (QFED) version 2.4 (Darmenov and Da Silva, 2015) with emission factors from Andreae (2019). Biogenic emissions of isoprene, monoterpenes, and methylbutenol are prescribed based on the Model of Emissions of Gases and Aerosols from Nature (MEGAN v2.1) inventory (Guenther et al., 2012). This inventory is used to account for the land cover changes (LCC) relying on satellite-based land cover distribution maps obtained by modifying the MODIS PFT dataset (MCD12Q1; Friedl and Sulla-Menashe, 2019) in order to match the reconstructed yearly tree cover distribution based on the Global Forest Watch dataset (Hansen et al., 2013), as detailed in Opacka et al. (2021).

Biogenic emissions of acetaldehyde and ethanol are parameterised following Millet et al. (2010), biogenic methanol emissions are from the MEGANv2.1 inventory and biogenic CO emissions are accounted for following Müller and Stavrakou (2005). Natural sources of NO_X are also prescribed. In particular, soil NO emissions are obtained from the dataset of Weng et al. (2020) generated with the Harvard-NASA Harmonized Emissions Component (HEMCO) version 2.1 model and rely on the parameterisation of Hudman et al. (2012). Alternative bottom-up inventories for BB and soil NO emissions will be evaluated through sensitivity tests. Given the large disparities in BB emissions among bottom-up inventories (Pan et al., 2020), the Global Fire Emissions Database (GFED4s; van der Werf et al., 2017) will be included in the analysis. Similarly, considering the large uncertainties in natural NO_X emissions, the in-house YL-ERA5 bottom-up inventory, based on the Yienger-Levy algorithm (Yienger and Levy, 1995) and driven by ERA5 meteorological fields will also be tested.

To investigate the variability and trends of HCHO columns across the African continent, we defined five regions, shown in Figure 4-1. These regions were selected to capture the diversity of emission sources, climatic conditions, and ecosystem types across Africa, thereby allowing for a more detailed and region-specific analysis of both interannual variability and long-term trends.

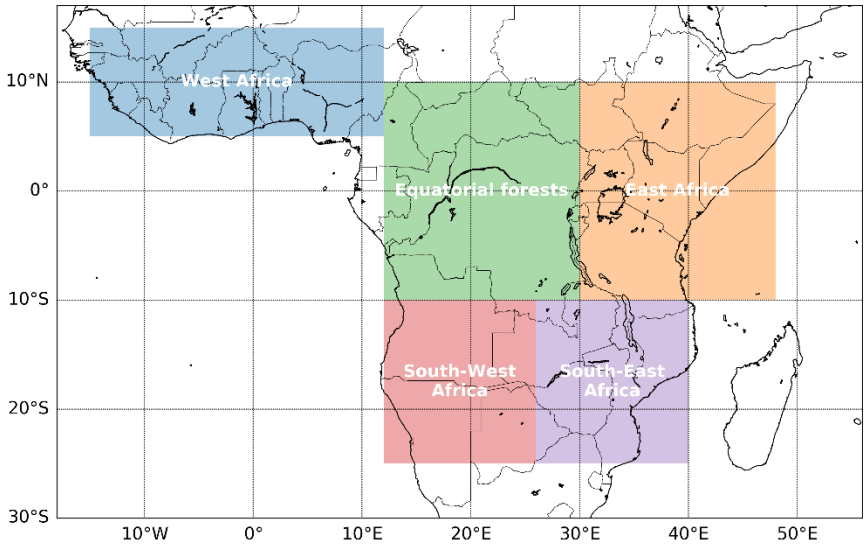


Figure 4-1: The African domain used in the study (30°S-17°N, 18°W-56°E), and selected regions defined as: (i) West Africa (15°W-12°E, 5°-15°N), (ii) Equatorial forests (12°E-30°E, 10°S-10°N), (c) East Africa (30°E-48°E, 10°S-10°N), (d) South-West Africa (12°E-26°E, 10°-25°S), and (e) South-East Africa (26°E-40°E, 10°-25°S).

4.5. Results and interpretation

4.5.1. Average HCHO columns, variability and trends

Figure 4-2 displays the spatial distribution of average HCHO columns over 2005-2018 in January and July, as retrieved from OMI CCI+ and simulated with MAGRITTE model. The modelled spatial distribution corresponds very well with the observations. The highest columns in OMI CCI+ are found over forested regions, Equatorial and West Africa, and biomass burning areas, and they display a clear seasonal pattern. In January, concentrations peak in the northern equatorial belt, while in July the maximum shifts southward, reflecting the fire season. This north-south shift of burning regions follows the migration of the Intertropical Convergence Zone (ICZ), which drives the alternation of rainy and dry seasons across Africa.

The model shows a positive bias over forested regions. For instance, in January, the modelled HCHO columns reach about 30×10^{15} molec. cm^{-2} in the vicinity of the Central African Republic, whereas OMI columns are around 20×10^{15} molec cm^{-2}. Conversely, the model exhibits a substantial underestimation over the savannas of the Southern Hemisphere.

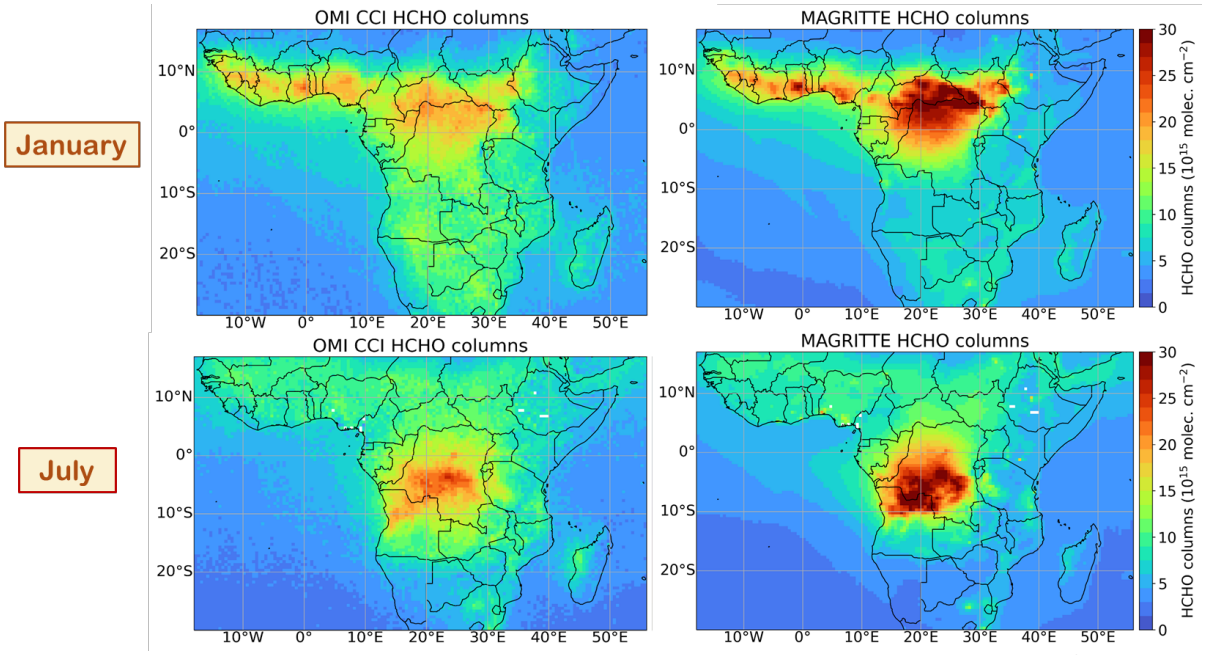


Figure 4-2: Spatial distribution of OMI CCI+ and MAGRITTE HCHO columns (in 10^{15} molecules cm^{-2}) in January (upper row) and July (lower row) averaged over 2005-2018.

Figure 4-3 illustrates the monthly variation of observed and simulated HCHO columns over a subset of the entire period, 2014-2017. The correlations are strong (~0.9) across most regions, except in East Africa, where the model accounts for 61% of the OMI variability. In West Africa (Figures 4-1 and 4-3a) the overall bias is very small (~-2%) and the observed amplitude of HCHO columns is well captured by the model. Over equatorial forests (Figures 4-1 and 4-3b), the model reproduces well the two wet and two dry seasons every year and overestimates HCHO columns during the dry seasons. East Africa (Figures 4-1 and 4-3c) shows generally low HCHO column densities (~8×10^{15} molec. cm^{-2}) with limited seasonal and interannual variability, and here, the model underpredicts columns by ~18%, likely due to missing or underestimated sources in this region. In southern Africa (South-West and South-East, Figures 4-1 and 4-3d-e), the model underpredicts HCHO columns throughout the year by nearly 30% relative to OMI CCI. Previous studies suggest that the underprediction in southern Africa is associated with an underestimation of isoprene emissions, likely due to underestimated basal emission rates of regional vegetation species (Marais et al., 2012; Opacka et al., 2025; Wells et al., 2020).

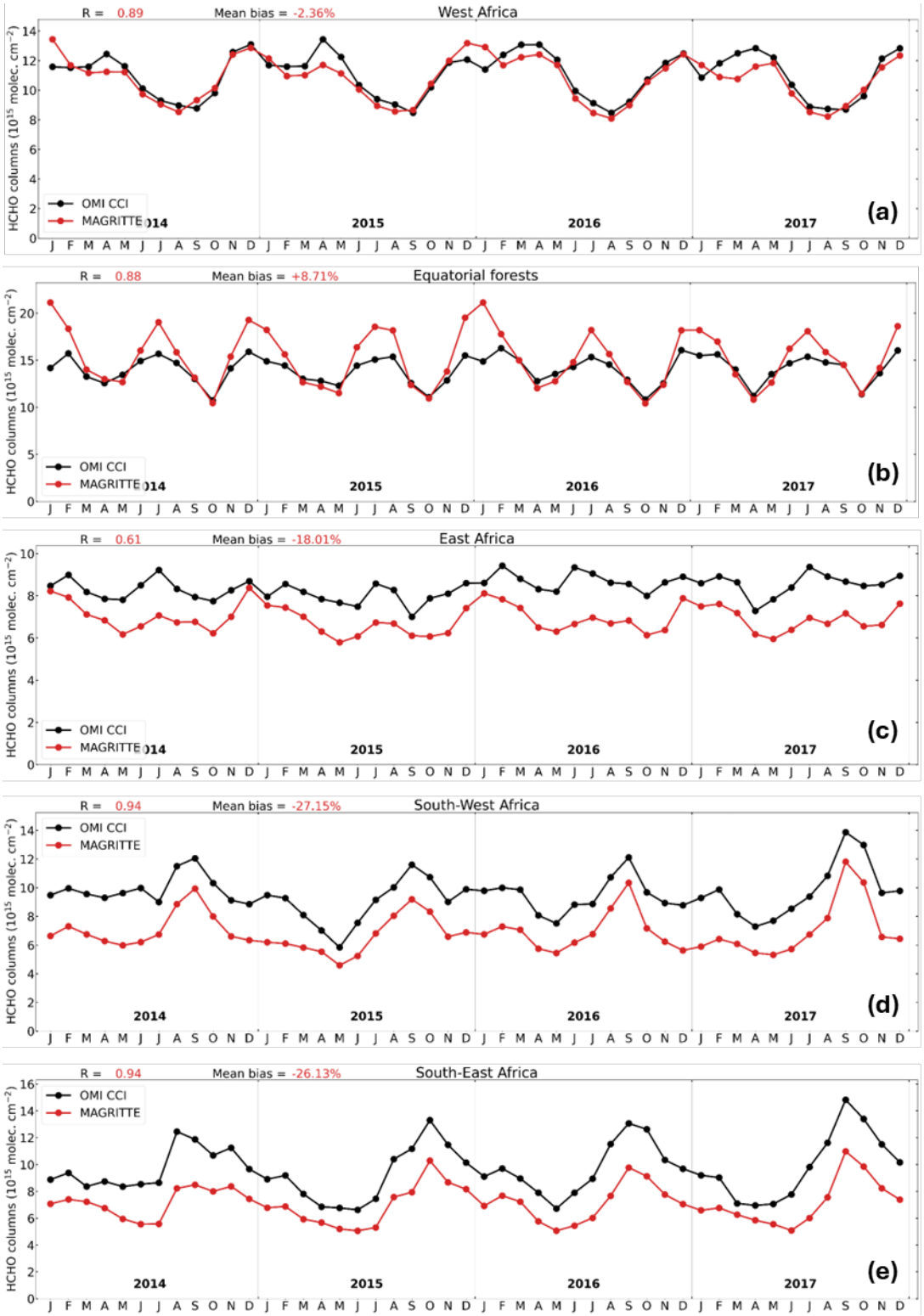


Figure 4-3: Monthly OMI CCI+ and MAGRITTE HCHO columns (in 10^{15} molecules cm^{-2}) over 2014-2017 averaged over the selected regions shown in Fig. 4- 1.

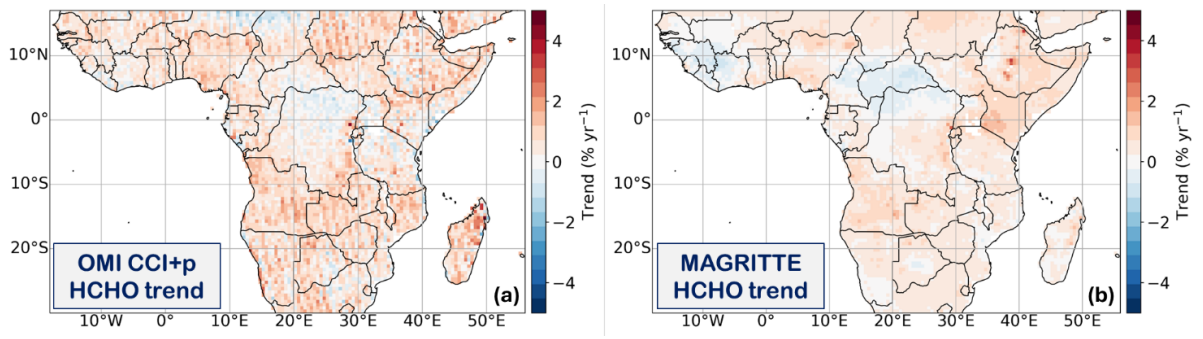


Figure 4-4: Spatial distribution of trends (% yr^{-1}) of (a) OMI CCI+ and (b) MAGRITTE HCHO columns over 2005-2018.

The spatial distribution of trends of OMI CCI+ HCHO columns over the 2005-2018 period shows predominantly positive trends across most of the African continent, with a few exceptions in Central African Republic and the Sahel (Figure 4-4). The simulated spatial distribution of trends is generally in good agreement, although weaker on average. Positive observed trends across African sub-regions range from +0.4% to +1% per year, cf. Table 4-1. The strongest regional trends in the satellite record are found in the South-West and South-East regions, ca. 0.8-0.9% yr^{-1}. MAGRITTE predicts slightly lower trends (0.6%yr^{-1}) in South-West Africa and nonsignificant trends in the South-East. West Africa exhibits slightly lower positive trends, 0.6% yr^{-1}. In the equatorial forests and East Africa, the observed trends are weaker (+0.4%yr^{-1}), partly due to the presence of localised negative trends in these regions. The calculated model trends are consistent with the observations in East Africa, mainly due to strong positive localised trends over major Ethiopian cities, Addis-Ababa and Jimma, but are not significant above equatorial regions.

Table 4-1: Regional trends (% yr^{-1}) from observed OMI CCI+ and modelled MAGRITTE HCHO columns over 2005-2018. Trends are calculated using the seasonal Mann-Kendall method.

Regions	OMI CCI trend (% yr^{-1})	MAGRITTE trend (% yr^{-1})
West Africa	0.6	0.2
East Africa	0.4	0.5
Equatorial forests	0.4	Not significant
South-West Africa	0.9	0.6
South-East Africa	0.8	Not significant

Table 4-2: Definition of wet and dry seasons per selected region based on the QFEDv2.4 fire inventory. The dry seasons coincide with peaks in biomass burning emissions.

Regions	WET	DRY
West Africa	May-September	January-March, November-December
East Africa	May-September	January-March, October-December
Equatorial forests	January-April October-December	May-September
South-West Africa	January-April November-December	June-October
South-East Africa	January-April, December	June-October

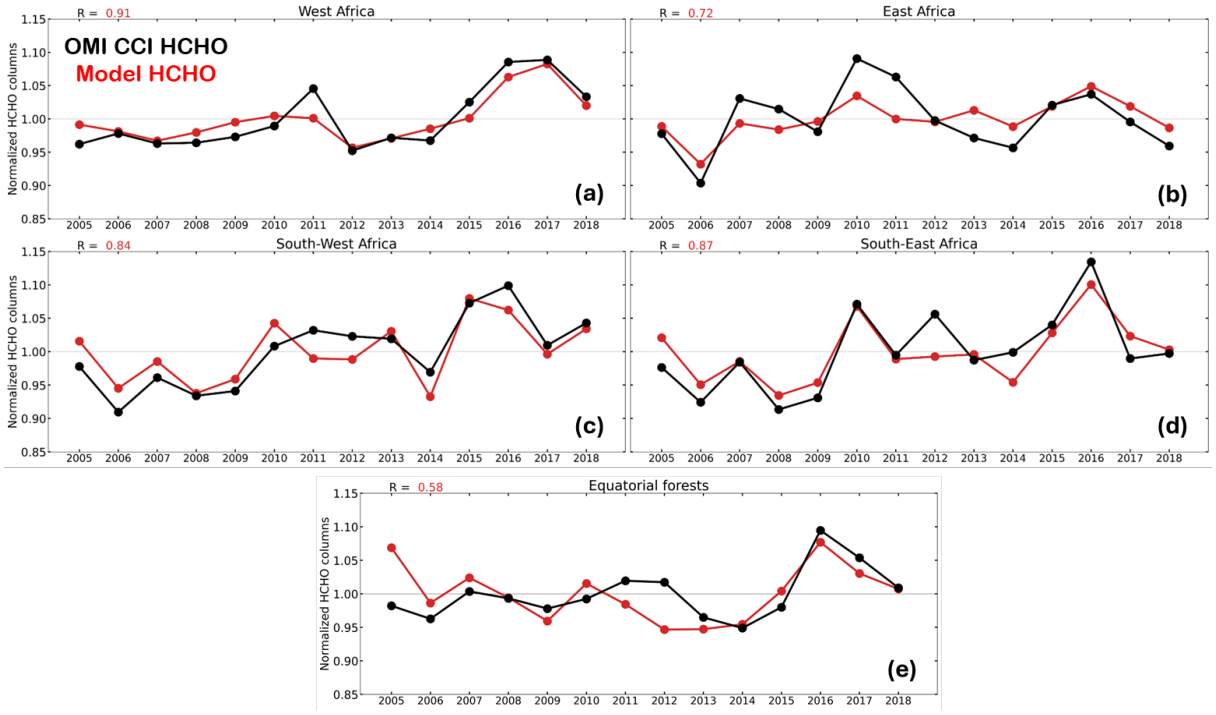


Figure 4-5: Seasonal averages of OMI CCI+ (black) and modelled (red) HCHO columns, normalised by the 2005-2018 mean seasonal average, over the regions of Fig. 4-1. Seasonal averages are calculated for the wet season of each region defined in Table 4-2. Correlation coefficients are given inset.

Figure 4-5 shows normalised interannual HCHO columns averaged over the wet season (Table 4-2) for each across the regions of Figure 4-1. The wet season variability is within 10% of the seasonal average values over 2005-2018. The model agrees well with the observations, with correlation coefficients exceeding 0.7 in all regions, demonstrating the model skill to reproduce the interannual HCHO variability in the wet season. Lower correlations are found in East Africa (0.72) and the equatorial forests (0.58) compared to other regions, where the model explains 84-91% of the observed HCHO variability. For example, in East Africa the model underestimates the HCHO peaks in 2007-2008 and 2010-2011 (Figure 4-5).

In the dry season (Figure 4-6), the model captures the interannual variability very well in East Africa (0.86), including the 2016 maximum associated with El Niño, and in South-West Africa (0.84). The correlations are lower in the other three regions, likely due to flaws in the distribution and magnitude of the bottom-up inventory for fires used in the model. An alternative biomass burning inventory should be tested in the future.

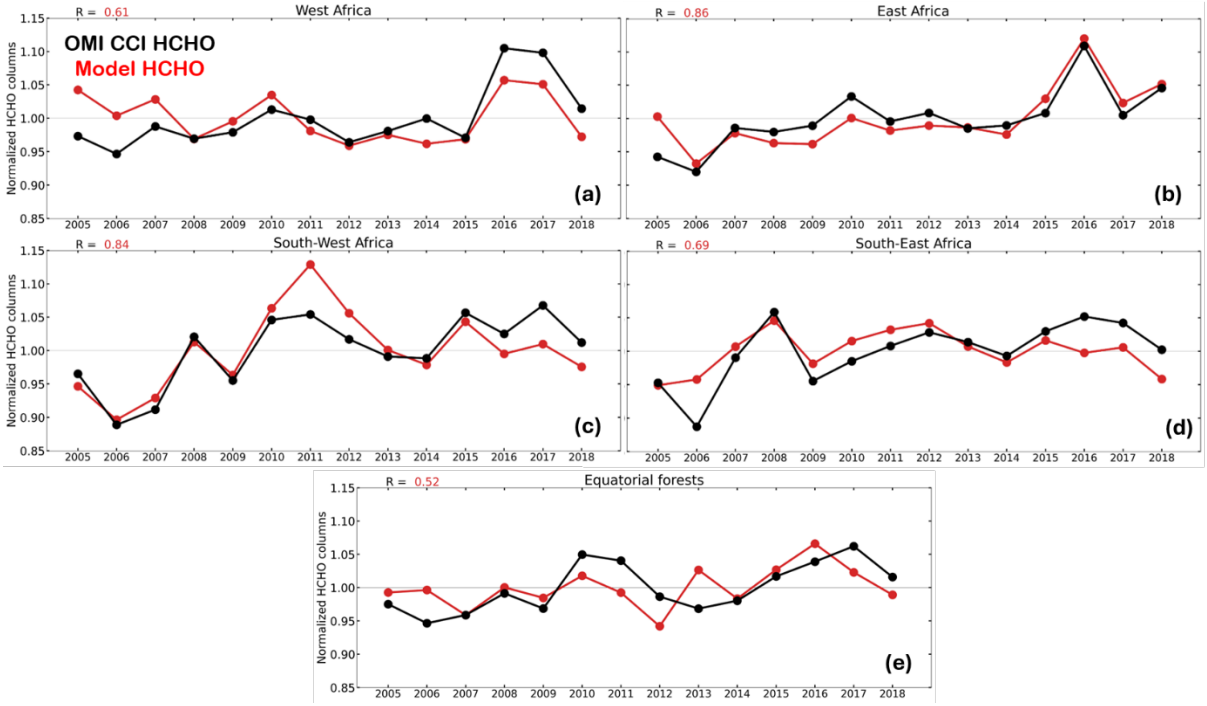


Figure 4-6: Seasonal averages of OMI CCI+ (black) and modelled (red) HCHO columns, normalised by the 2005-2018 mean seasonal average, over five regions (Fig. 4-1). Model results correspond to the standard simulation including all sources. Seasonal averages are shown for the dry season (Table 4-2). Correlation coefficients are given in the top left of each panel.

4.5.2. Contributions to HCHO columns from individual sources

Figure 4-7 illustrates the spatial distribution of trends of the individual VOC sources from bottom-up inventories used in the MAGRITTE multiyear simulations. The anthropogenic VOC emission trends are predominantly positive across the continent, with the exception of Namibia and South Africa. Biomass burning emissions display strong negative trends across the northern equatorial belt stretching from west to east, particularly over Côte d'Ivoire, Togo and Nigeria. In contrast, relatively strong emission trends persist over equatorial forests, especially in the Democratic Republic of Congo. Isoprene exhibits positive trends across central Africa (Central African Republic, Democratic Republic of Congo), with enhanced increases over southern Sudan and northern South Sudan, as well as over southern Africa (Namibia, Zambia, Botswana and South Africa). These trends are primarily driven by temperature trends due to climate change, while land cover changes contribute to localised enhancements (Figure 4-7d). In western Africa, in particular, strong negative trends are linked to deforestation in the region.

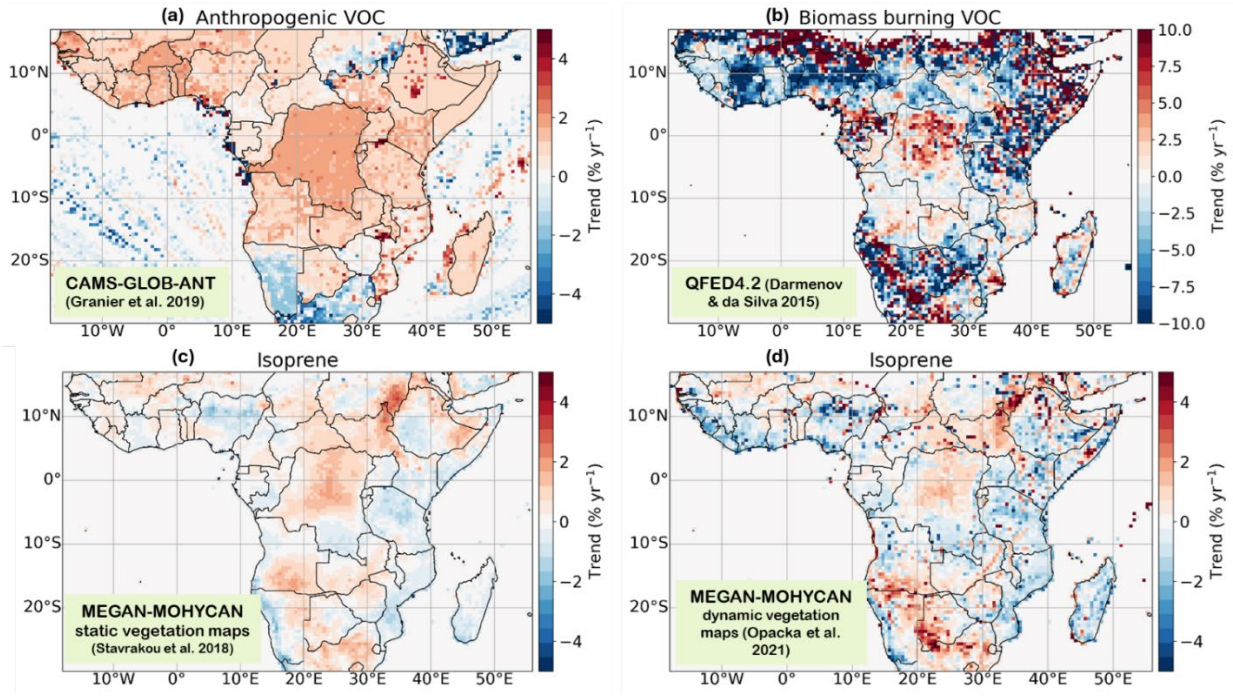


Figure 4-7: Trend maps over 2005-2018 of different bottom-up VOC emission sources used in MAGRITTE simulations: (a) anthropogenic CAMS-GLOB-ANT, (b) biomass burning QFEDv4.2 and isoprene (biogenic) MEGAN-MOHYCAN using (c) static (Stavrakou et al., 2018) and (d) dynamic vegetation maps (Opacka et al., 2021).

The MAGRITTE model enables numerical sensitivity test by selectively switching off different VOC sources, thereby quantifying their relative contributions to HCHO columns. A major contribution stems from the background, a ubiquitous and relatively uniform source of HCHO from CH_4 oxidation. The background source accounts for a substantial fraction (50-60%) of the total column, except for equatorial forests where biogenic emissions dominate (47%) due to the large isoprene fluxes from tropical forests, cf. Table 4-3. In other regions, biogenic sources contribute 22-28% of HCHO production, while biomass burning contributes mainly to the regions of the Southern Hemisphere. Overall, the full model simulation systematically underestimates HCHO compared to bias-corrected OMI CCI+ observations across all regions, with biases of about -11% over equatorial forests and -18% over West Africa (not shown). This bias-correction (1.33 x OMI - 1.2 10^{15} molec. cm^{-2}) is derived by the validation teams of the ESA CCI+ project, based on independent FTIR column observations of HCHO from a large number of sites worldwide.

Table 4-3: Relative contributions (in percentage) of background (CH_4-oxidation), biogenic and biomass burning sources to the modelled HCHO columns averaged over 2005-2018.

Regions	Background (%)	Biogenic (%)	Biomass burning (%)
West Africa	58	25	7
East Africa	63	22	8
Equatorial forests	35	47	18
South-West Africa	55	28	15
South-East Africa	61	25	11

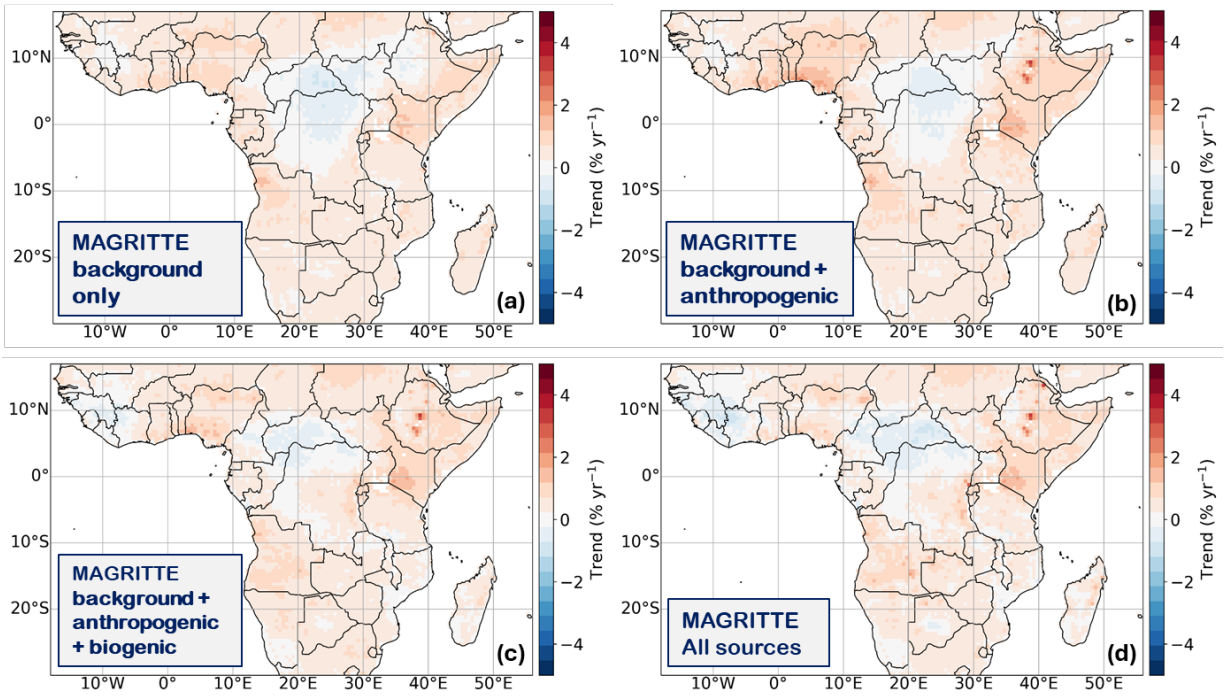


Figure 4-8: Spatial distributions of MAGRITTE simulated HCHO trends for (a) the background source only, (b) as in (a) but with additional anthropogenic sources (background + anthropogenic), (c) as in (b) but with additional biogenic sources (background + anthropogenic + biogenic), and (d) as in (c) all sources (including biomass burning).

Overall, the observed trends (Figure 4-4a) are largely explained by the background source, which provides the dominant contribution across most regions (Figure 4-8a). In Ethiopia, however, stronger positive trends are driven by the positive anthropogenic VOC emission trends in the major cities Addis Abeba and Jimma (Figure 4-8b). Biogenic emission trends are comparatively small, but their inclusion improves the agreement between modelled and observed patterns over the Congo Basin, where tropical forests are a major source of isoprene (Figure 4-8c). In contrast, the model simulates negative trends over western Africa, mainly linked to decreasing fire emissions and biogenic fluxes. These trends are not supported by the observations, highlighting potential shortcomings in the representation of biomass burning and land-cover changes in the inventories used. Alternatively, the discrepancies may arise from uncertainties in OH levels, which strongly influence oxidation processes and consequently, HCHO production. The following section investigates these potential

shortcomings in West Africa through an analysis of alternative bottom-up inventories for biomass burning VOC and soil NO emissions.

4.5.3. Sensitivity analysis: Biomass burning VOC and soil NO inventories

To assess the sensitivity of our results to the choice of biomass burning inventory, we performed a test by replacing the QFED inventory with GFEDv4. Both inventories exhibit consistent spatial patterns in VOC trends, which is expected given that they are both based on MODIS fire products. GFED relies primarily on burned area and active fires counts, while QFED uses fire radiative power and aerosol optical depth. In West Africa, QFED estimates BB VOC emissions of 5.34 Tg yr^{-1} over 2005-2018, with a decreasing trend of -2.8% yr^{-1} (Figure 4-7a). GFED provides slightly lower estimates (4.12 Tg yr^{-1} and -2.6 %yr^{-1}) and shows a different annual variability e.g., 2005-2008 or the 2016 peak in GFED missing in QFED. The use of GFEDv4 is found to have a small impact on the modelled HCHO trends in West Africa (Figure 4-9).

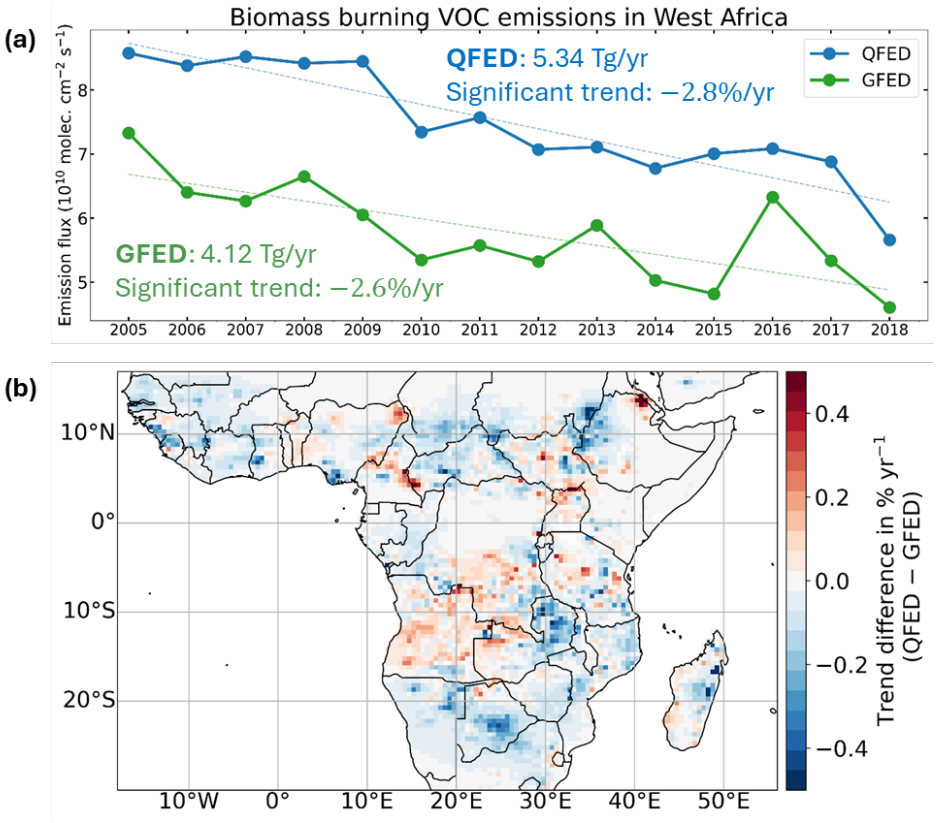


Figure 4-9: (a) Annual VOC emissions in two BU inventories QFED (blue) and GFED (green) averaged over West Africa and (b) difference in simulated HCHO trends (%yr^{-1}) when using QFED or GFED as BB BU inventory.

Uncertainties in OH levels can be partly attributed to soil NO_X emissions, since NO_X plays a key role in OH production through photochemical reactions. At the surface, OH concentrations are strongly influenced by NO fluxes originating from microbial activity in the upper soil layers, a process that remains highly uncertain. To assess this impact, we compared two bottom-up

inventories of soil NO emissions: HEMCO and YL-ERA5. Figure 4-10 shows the trend map in Africa for both inventories, as well as their influence on HCHO column trends.

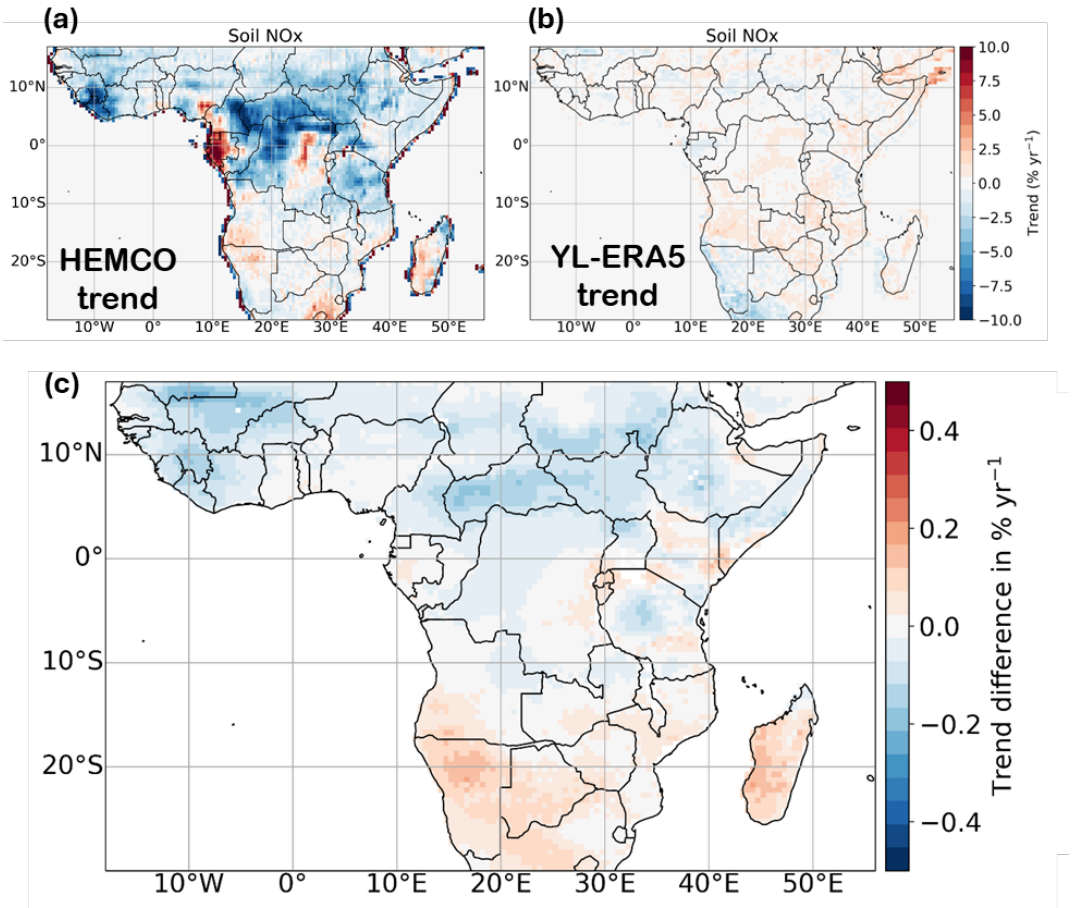


Figure 4-10: Spatial distribution of trends in (a) HEMCO and (b) YL-ERA5 soil NO emissions, and the difference (HEMCO – YL-ERA5) in simulated HCHO trends (in % yr^{-1}).

The comparison reveals large discrepancies between the two datasets. The HEMCO inventory exhibits a strong negative overall trend in African soil NO emissions (-1.3% yr^{-1}), whereas YL-ERA5 shows no significant trend (Figure 4-10a-b). HEMCO indicates negative soil NO trends across western Africa (e.g., Liberia, Guinea), and much of the equatorial forests, except along the western coast (Gabon, Equatorial Guinea, southern Cameroon), where strong positive trends are apparent. These differences have direct implications for OH levels: a negative trend in soil NO reduces boundary layer OH (Figure 4-11), thereby inducing a negative trend in HCHO columns over regions with strong biogenic and pyrogenic VOC emissions, particularly in the Northern Hemisphere savannas.

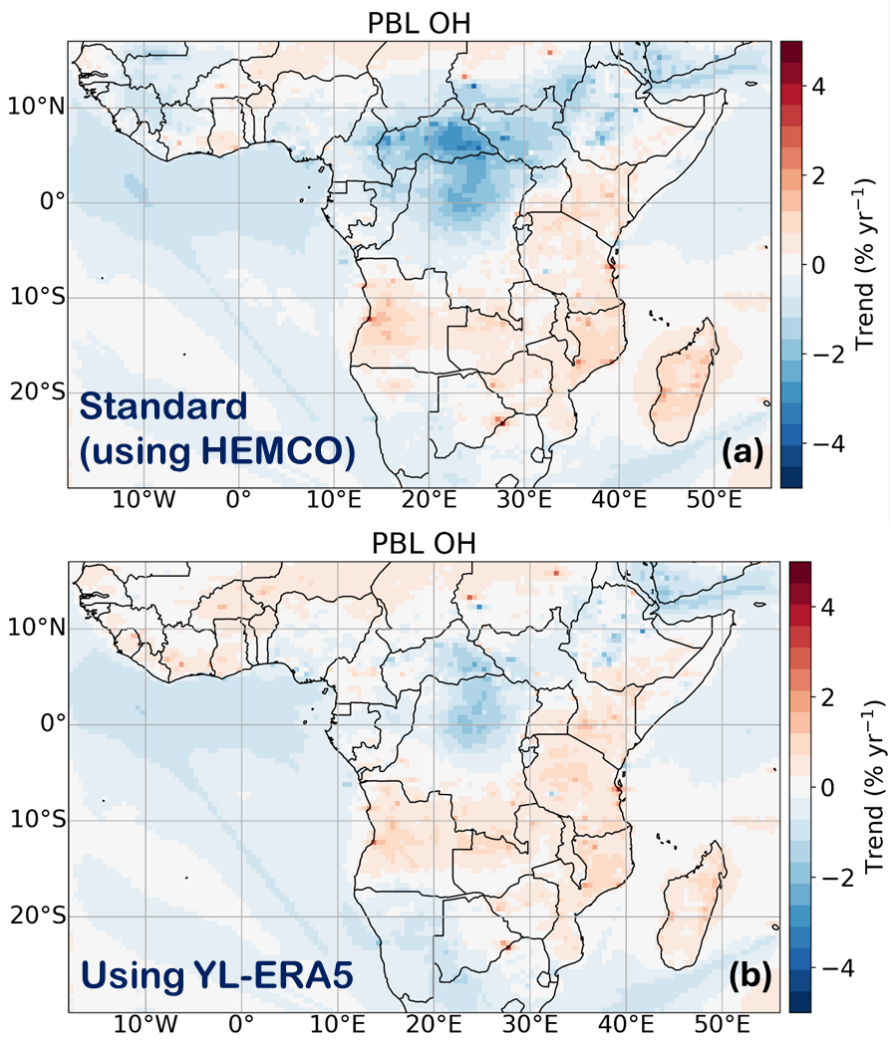


Figure 4-11: Spatial distribution of planetary boundary layer (PBL) OH concentrations (in % yr^{-1}) over 2005-2018, based on two soil NO inventories: (a) HEMCO, as in the standard simulation and (b) YL-ERA5.

Over the equatorial forests, the simulated negative trend in PBL OH is primarily driven by three factors: the increase of CH_4 levels, the increase in isoprene fluxes, and the decreasing soil NO fluxes as represented by the HEMCO inventory (Figure 4-11a). Together, these processes reduce the oxidative capacity of the boundary layer and contribute to a pronounced decrease in modelled HCHO columns throughout the years. In contrast, slightly positive OH trends are simulated in other regions, largely because of the negative trend in isoprene emissions (Figure 4-8c-d) outweigh the opposing influence positive PBL OH trend due to CH_4 oxidation (Figure 4-8a). The treatment of soil NO emissions in the model proves to play a key role. Trends in soil NO directly affect OH production, thereby exerting a first-order control on modelled HCHO variability. In fact, approximately half of the simulated negative HCHO trend over equatorial forests can be attributed to the strong negative soil NO trend prescribed by the HEMCO inventory.

4.6. Conclusion and perspectives

We have performed long-term (2005-2018) simulations with the regional CTM MAGRITTE at 0.5°x0.5° to assess and evaluate long-term tropospheric OMI CCI+ HCHO columns variability and trends across the continent and at regional scales.

Overall, the model reproduces the observed OMI trends well when all emission sources are included, although the simulated trends are generally lower, for reasons that remain unclear. A dominant contribution to the HCHO columns is due to CH_4 oxidation, except over tropical forests where the HCHO formation from the oxidation of biogenic emissions is more significant. The background source, largely controlled by CH_4, OH, and hence by NO_X, explains a substantial part of the observed OMI trend. Biogenic emission trends, while having only a modest overall impact, improve the agreement between model and observations. In contrast, the soil NO_X source emerges as particularly significant, exerting a strong influence on the predicted HCHO trends. Importantly, the model captures well the observed interannual variability of HCHO during both wet and dry seasons, with correlation coefficients exceeding 0.7 across all regions, highlighting its ability to capture the temporal variability despite remaining uncertainties in trend magnitude.

Future work could focus on several avenues to refine our understanding of HCHO trends. First, the trend of the L3 CCI+ products should be investigated in detail to assess consistency with current findings. The impact of bias correction on satellite-model comparisons warrants further evaluation, as it may affect the magnitude of the observed columns. The use of alternative inventories for anthropogenic emissions could improve the representation of recent years and help resolve discrepancies between modelled and observed trends. Extending the analysis beyond 2018 would provide insights into more recent changes and the influence of evolving emission patterns. Finally, combining HCHO observations with CCI+p NO_2 data (Glissenaar et al., 2025), as explored in the Progress in the Interpretation of Remotely-sensed Atmospheric climate products using Modelling, Inversion and Data assimilation (PIRAMID) project (ESA ITT AO/1-12469/24/I-LR), could allow for a more comprehensive assessment of atmospheric oxidation processes and a better constraint on OH levels.

5. IASI/MOPITT/TROPOMI CO total column comparison

5.1. Introduction and context

To account for TROPOMI data in the project, the team first proposed to generate TROPOMI L3 grids (Precursors_cci+_Negotiation_meeting_minutes_01_00) but it was then decided that a few pages of comparison of the CO distribution of IASI, MOPITT and TROPOMI would be more suitable as the Level 3 TROPOMI monthly grids can easily be generated from Level 2 available on line (https://sentinels.copernicus.eu/web/sentinel/data-products/-/asset_publisher/fp37fc19FN8F/content/sentinel-5-precursor-level-2-carbon-monoxide).

This study is not a validation, but a comparison of 6.5 years of IASI, MOPITT and TROPOMI CO data, based on timeseries over different latitude bands as well as seasonnal maps in order to get seasonal biases. The data used in the comparison are first presented in Section 5.2, then the comparison is given in Section 5.3 and 5.4. A regional trend analysis is also included in

Section 5. At last, a summary of Antje Inness paper published in ACP in 2022 is given in Section 5.6.

For this comparison, we focused on the period 1 May 2018-31 Dec 2024 and used the data presented in Table 5-1. Note that two TROPOMI products are available: «all-sky» and «clear-sky». Here, we used TROPOMI clear-sky data, to be comparable with IASI and MOPITT retrievals where the retrieved pixels are not considered contaminated by clouds. The different spatial coverage for half a day (daytime) for each product can be seen in Figure 5-1. In this study, only data between 70°S and 70°N are considered, since high-latitude regions are not of primary interest for CO studies. These regions are typically filtered out in the assimilation schemes.

Table 5-1*: Description of the IASI, MOPITT and TROPOMI L2 CO products used for this comparison.*

	IASI (Metop-B and -C)	**MOPITT (Terra)**	**TROPOMI (Sentinel-5P)**
Instrument type	Fourier Transform Spectrometer	Gas Correlation Radiometer	UVNS spectrometer
Overpass time (LT)	09:30 a.m. and p.m.	10:30 a.m. and p.m.	01:30 p.m.
Spectral range for CO	2143-2181.25 cm^{-1} (TIR)	TIR	4329-4273.50 cm^{-1} (SWIR)
Pixel resolution (swath width)	12 km diameter at nadir (~ 2200 km)	22x22 km (~ 640 km)	7×5.5 km (~ 2600 km) Before 2019-08: 7x7km
Retrieval method	Optimal Estimation Method (FORLI)	Optimal Estimation Method (MOPFAS)	Tikhonov regularization (SICOR)
L2 data version	FORLI V6.7	9T	RPRO V2 2018-2022/07/25
Data filtering	Solar zenith angle < 90°, COTC error < 7.5%, QF=2, cloud cover < 25%	Solar zenith angle < 90°, no Pixel 3, 5A SNR > 1000, RetrievalAnomalyDiagnostic = all at 0	Solar zenith angle < 80° Clear-sky data only (QA=1)
Data availability	https://iasi.aeris-data.fr/	https://www.earthdata.nasa.gov	https://sentinels.copernicus.eu/web/sentinel/data-products/-/asset_publisher/fp37fc19FN8F/content/sentinel-5-precursor-level-2-carbon-monoxide
DOI	https://doi.org/10.25326/64 and https://doi.org/10.25326/65	https://doi.org/10.5067/TERRA/MOPITT/MOP02T.009	https://doi.org/10.5270/S5P-bj3nry0

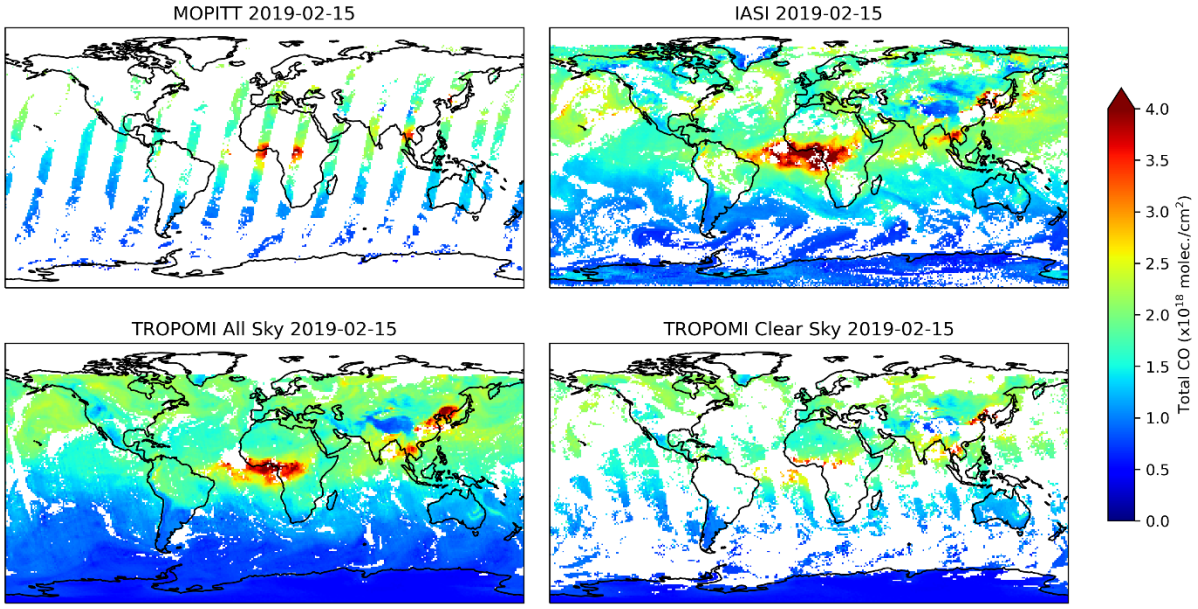


Figure 5-1: Spatial distribution for day time (half a day) of 15 Feb. 2019 for MOPITT, IASI B and C, as well as TROPOMI (all-sky and clear-sky). Only TROPOMI clear-sky data are used in this comparison. To perform the comparison, we first gridded daily data in 1°x1° grids.

5.2. Timeseries over different latitude bands

The time series of total CO columns from IASI, MOPITT, and TROPOMI over different latitude bands (Figure 5-2) shows that the three products capture consistent seasonal cycles and long-term variability, including recurrent biomass burning peaks and interannual fluctuations. IASI (light blue) generally reports the highest CO values, MOPITT (black) the lowest, and TROPOMI (purple) lies in between, tracking the seasonal cycles closely but with slightly lower amplitudes compared to IASI. The patterns are particularly clear in the tropics, where strong fire signals dominate, and in the Northern Hemisphere mid-latitudes, where anthropogenic emissions and seasonal transport play a key role.

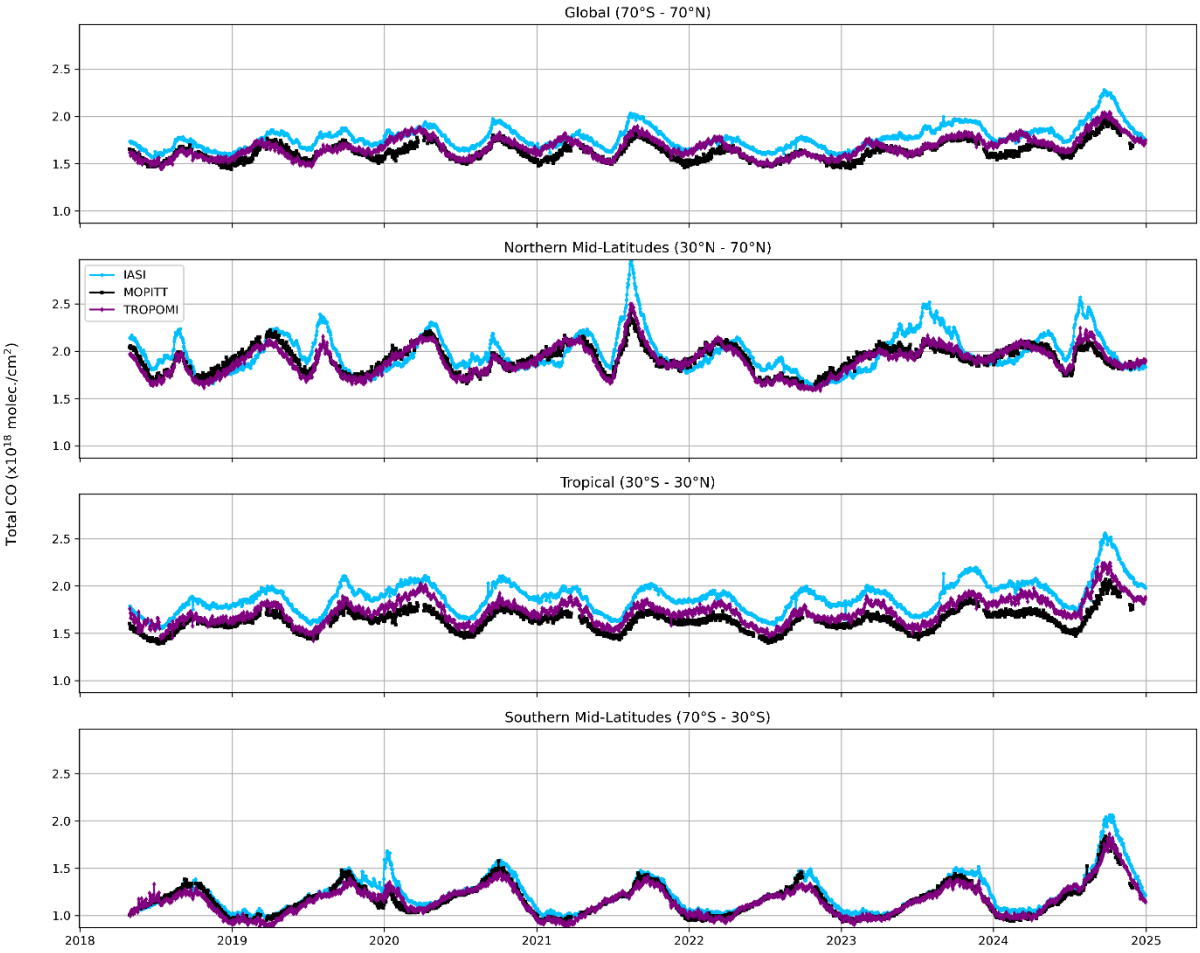


Figure 5-2: ***Time series of total column CO (×10¹⁸ molec./cm²) from IASI (light blue), MOPITT (black), and TROPOMI (purple) for the period 2018–2025. Panels show global (70°S–70°N), Northern Hemisphere mid-latitudes (30°N–70°N), tropics (30°S–30°N), and Southern Hemisphere mid-latitudes (70°S–30°S).***

The mean relative biases table (Table 5-2) confirm these systematic differences. Globally, IASI columns are on average 9% higher than MOPITT, whereas TROPOMI is 5.7% lower than IASI and 2.7% higher than MOPITT, again placing it between the two. The largest discrepancies occur in the tropics, where IASI exceeds MOPITT by nearly 15%, possibly due to stronger mid-tropospheric sensitivity over intense burning regions (we are currently examinating this difference). In contrast, biases are smaller at mid-latitudes (3–4%), and in both hemispheres TROPOMI agrees closely with MOPITT (−0.8%).

Table 5-2: ***Mean relative biases (%) of total column CO between IASI, MOPITT, and TROPOMI for the period 2018–2025, calculated globally and by latitude band.***

	Mean_Rel_IASI-MOPITT (%)	Mean_Rel_TROPOMI-IASI (%)	Mean_Rel_TROPOMI-MOPITT (%)
Global (70°S - 70°N)	9.0	-5.7	2.7
Northern Mid-Latitudes (30°N - 70°N)	3.4	-3.6	-0.8

Tropical (30°S - 30°N)	14.9	-7.9	5.8
Southern Mid-Latitudes (70°S - 30°S)	4.5	-5.2	-0.8

5.3. Seasonal comparison

The seasonal mean CO total column maps from IASI, MOPITT, and TROPOMI presented in Figure 5-3 highlight both common large-scale patterns and differences between the instruments. All three products capture the strong seasonal signals associated with biomass burning and anthropogenic emissions, such as enhanced columns over central Africa in DJF and JJA, over Southeast Asia in MAM, and over South America in SON. These regional large concentrations are consistently detected across the instruments, but their magnitude differs: MOPITT generally reports lower total CO compared to IASI, while TROPOMI often lies in between the two, with stronger sensitivity to near-surface enhancements.

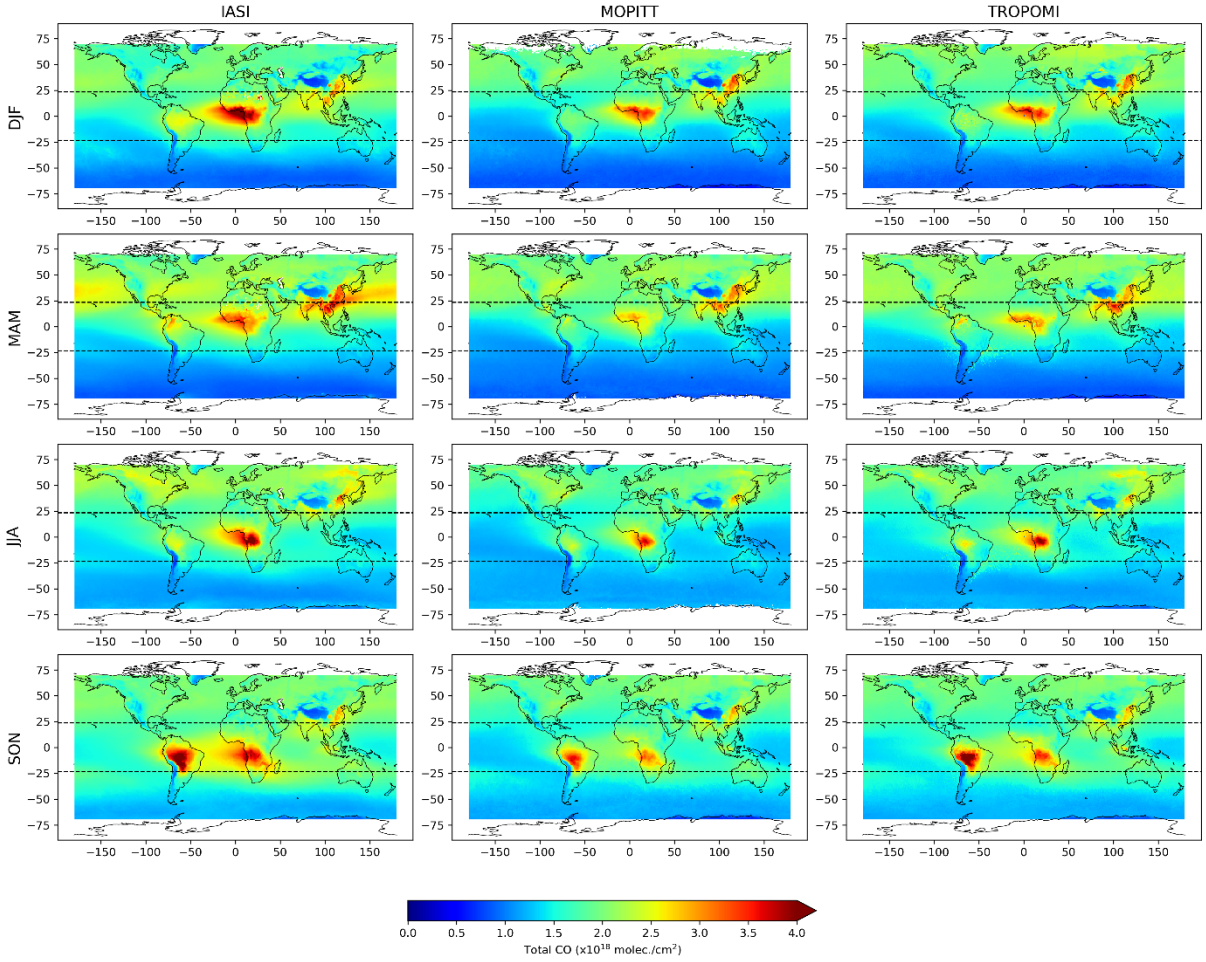


Figure 5-3: ***Seasonal distributions (DJF, MAM, JJA and SON) for IASI (column 1), MOPITT (column 2) and TROPOMI (column 3). Data above 70° of latitude have been masked. Dash lines indicate the Tropics (for biases calculated by latitude bands in Table Table 4.***

The relative bias statistics presented in Table 5-3 confirm these systematic offsets. IASI columns are about 9–11% higher than MOPITT throughout the year, with little seasonal variation. TROPOMI, by contrast, shows a negative bias relative to IASI (−3.7% in DJF to −5.9% in SON), but a positive bias relative to MOPITT (+3.8% to +4.5%). This implies that TROPOMI consistently bridges the gap between the higher IASI and lower MOPITT columns. The slightly stronger negative bias against IASI in SON (−5.9%) coincides with the South American biomass burning season, visible in the maps as very pronounced enhancements. This suggests that differences in vertical sensitivity (TROPOMI being more responsive to boundary-layer emissions, IASI to mid-tropospheric signals) may partly explain the seasonal divergence.

Table 5-3: ***Mean Relative biases for (IASI-MOPITT)/MOPITT in column 2, (TROPOMI-IASI)/IASI in column 3 and (TROPOMI-MOPITT)/MOPITT in column 4.***

Season	Mean_Rel_IASI-MOPITT (%)	Mean_Rel_TROPOMI-IASI (%)	Mean_Rel_TROPOMI-MOPITT (%)
DJF	10.22	-3.66	4.47
MAM	9.48	-4.58	4.22
JJA	10.34	-5.2	4.3
SON	10.79	-5.93	3.79

The latitude-dependent bias statistics presented in Table 5-4 reveal important regional differences that are not visible in the global means alone. In the Southern Hemisphere (lines highlighted in yellow), IASI consistently reports substantially higher CO than MOPITT, with relative biases reaching +14% in DJF and remaining positive across all seasons (+1.7 to +10.3%). TROPOMI reduces this discrepancy, showing a negative bias relative to IASI (−0.4% to −7.3%) but still remaining slightly higher than MOPITT (+1.4% to +5.5%). This suggests that in regions dominated by biomass burning emissions, such as Southern Africa and South America, TROPOMI again bridges the gap between IASI's higher and MOPITT's lower column values. In the Northern Hemisphere (lines highlighted in green), it is more variable : in DJF, IASI even shows a slight negative bias compared to MOPITT (−2.2%), but in MAM, JJA, and SON the bias becomes positive again, peaking at +13.5% in JJA. TROPOMI follows a consistent pattern of lying between the two datasets, with biases of about −2.6% to −8.9% relative to IASI and +1.0% to +3.2% relative to MOPITT. The larger contrasts in the north during summer (JJA) likely reflect stronger sensitivity differences between the SWIR (TROPOMI) and TIR (IASI/MOPITT) retrievals under high solar illumination and variable surface conditions.

Table 5-4: ***Same as Table 5-3 but divided by latitudes bands (South, Tropics and North)***

Season	Band	Mean_Rel_IASI-MOPITT (%)	Mean_Rel_TROPOMI-IASI (%)	Mean_Rel_TROPOMI-MOPITT (%)
DJF	South	14.03	-7.26	5.45

DJF	Tropics	17.75	-9.68	6.12
DJF	North	-2.15	5.91	1.53
MAM	South	4.72	-2.35	2.53
MAM	Tropics	18.21	-7.69	9.01
MAM	North	5.45	-3.72	1.1
JJA	South	1.68	-0.36	1.37
JJA	Tropics	15.64	-6.31	8.25
JJA	North	13.51	-8.94	3.22
SON	South	10.33	-5.69	3.7
SON	Tropics	18.12	-9.54	6.67
SON	North	3.94	-2.62	0.99

Overall, this latitude-banded analysis reinforces the global picture: IASI tends to report higher CO columns than MOPITT, particularly in the Southern Hemisphere, while TROPOMI consistently provides intermediate values, closer to MOPITT in the north and closer to IASI in the south.

5.4. Regional trend analysis

Temporal variations and trends in CO concentrations were examined across several regions, with particular focus on the North China Plain (30°–40° N, 110°–123° E) and the Amazon Basin (17°–2° S, 68°–53° W). These regions were selected because the North China Plain is largely influenced by anthropogenic CO emissions, whereas the Amazon region is characterized by recurrent biomass burning events.

Figure 5-4 shows the monthly time series of CO concentrations from IASI, TROPOMI, and MOPITT over the regions of interest, with monthly averages computed for days with simultaneous observations from all three instruments. The corresponding relative bias statistics are given in Table 5-5.

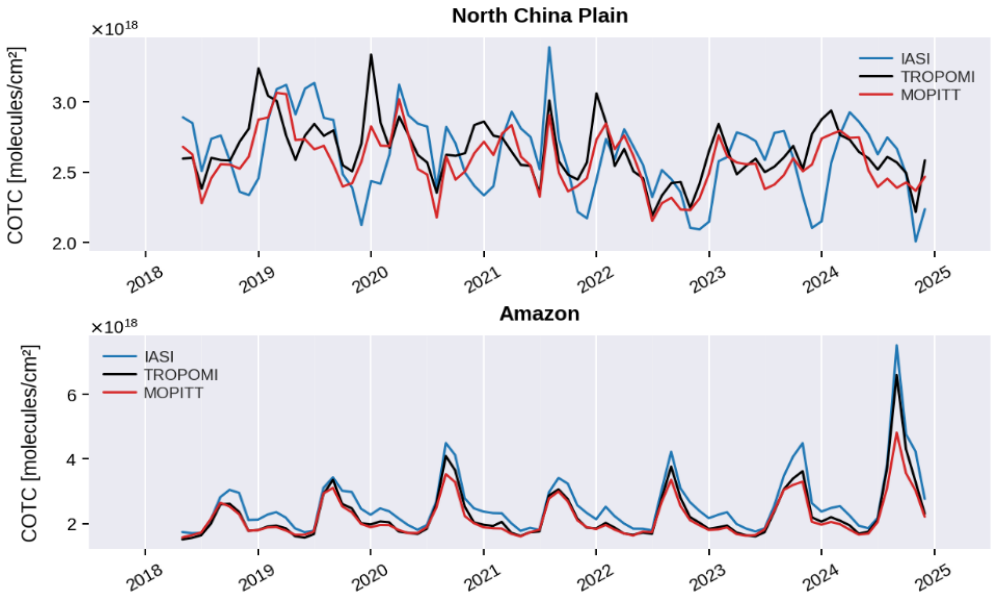


Figure 5-4: ***Monthly time series of CO concentrations calculated over the North China Plain (top panel) and the Amazon region (bottom panel) for IASI (blue), TROPOMI (black) and MOPITT (red), from May 2018 to December 2024.***

Table 5-5: ***Average relative biases for (IASI-MOPITT)/MOPITT, (TROPOMI-IASI)/IASI and (TROPOMI-MOPITT)/MOPITT, for the North China Plain and Amazon regions.***

Region	Mean_Rel_IASI-MOPITT (%)	Mean_Rel_TROPOMI-IASI (%)	Mean_Rel_TROPOMI-MOPITT (%)
North China Plain	3.47	3.01	4.86
Amazon	18.07	-11.57	3.96

From Figure 5-4 and Table 5-5, we note that over the North China Plain, the instruments exhibit good overall agreement. The mean relative biases are small, ranging from 3.01% (TROPOMI–IASI) to 4.86% (TROPOMI–MOPITT), indicating that all three datasets capture the temporal variability of CO concentrations in this region consistently. Over the Amazon Basin, larger discrepancies are observed: IASI shows a positive mean relative bias of 18.07% with respect to MOPITT, whereas TROPOMI exhibits a negative bias of −11.57% relative to IASI. Nevertheless, the relative bias between TROPOMI and MOPITT remains small (3.96%).

Figure 5-5 presents the monthly time series of CO anomalies from the three instruments, along with their corresponding linear trends. Trends were estimated using the Weighted Least Squares (WLS) linear regression method over the May 2018–May 2024 period. To reduce the influence of seasonal variability, the analysis was performed on monthly averaged anomalies, which were computed relative to the 2018–2024 monthly climatology and including only days with coincident observations from all three instruments. The monthly variance of CO concentrations was used as a weighting factor in the regression, thereby minimizing the

impact of outliers on the trend estimates. Table 5-6 summarizes the trend values obtained for each instrument over the regions of interest using the WLS method.

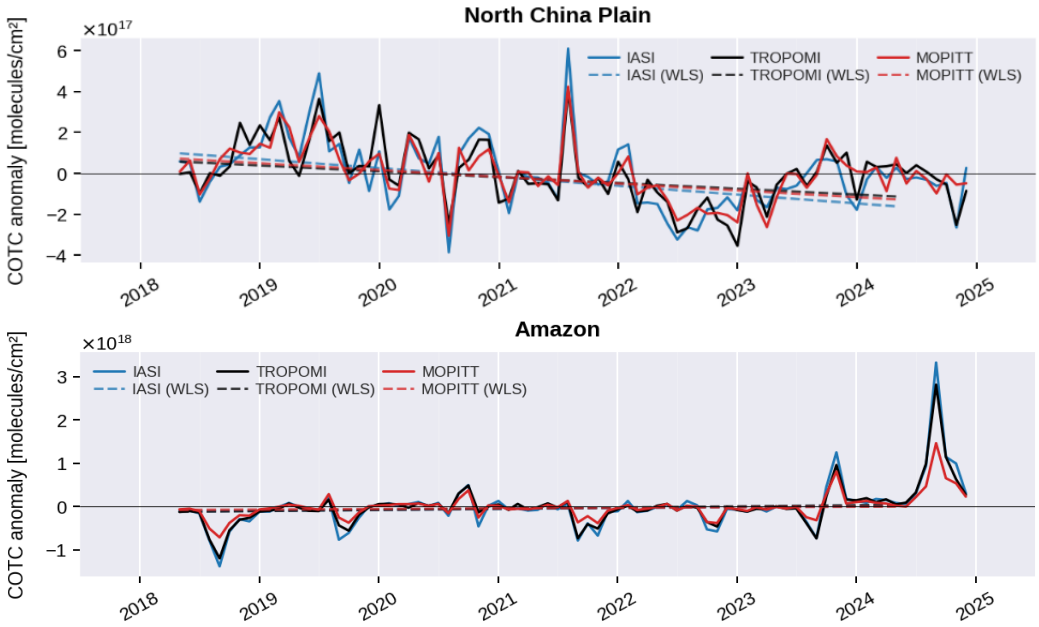


Figure 5-5: ***Monthly time series of CO anomalies from IASI (blue), TROPOMI (black) and MOPITT (red) and their associated linear trend (dotted lines) for the North China Plain (top panel) and Amazon regions (bottom panel).***

Table 5-6: ***CO trends values and their associated standard error in %/year estimated using the WLS regression method for the regions of interest. Significant trends to one standard-error are marked by an asterix (*).***

	North China Plain	Amazon
IASI	-1.53 ± 0.1*	0.87 ± 0.1*
MOPITT	-1.22 ± 0.1*	0.62 ± 0.2
TROPOMI	-1.07 ± 0.1*	1.15 ± 0.1*

From Figure 5-5 and Table 5-6, a strong and significant trend in CO concentrations over the North China Plain is observed by all three instruments. This decrease is attributed to the reduction in anthropogenic emissions following the deployment of China's "**Air Pollution Prevention and Control Action Plan"** in 2013 (Zheng et al., 2019[a]). In the Amazon region, all three instruments indicate positive CO trends, although statistically significant increases are observed only for IASI and TROPOMI. This rise in CO concentrations is consistent with the increased fire activity reported in the region during 2024 (Friedlingstein et al., 2025[b]). Although the 2018–2024 period is relatively short for robust trend estimation, all three instruments exhibit consistent trends of similar magnitude across the regions of interest.

[a] https://essd.copernicus.org/articles/11/1411/2019/
[b] https://essd.copernicus.org/articles/17/965/2025/essd-17-965-2025.html

5.5. Summary of Antje Inness ACP paper: Assimilation of S5P/TROPOMI carbon monoxide data with the global CAMS near-real-time system (2022)[c]

Inness et al. (2022) present a comprehensive assessment of the impact of assimilating CO total column (TCCO) observations from three satellite instruments—IASI, MOPITT, and TROPOMI—within the CAMS 4D-Var system. The three products differ significantly in their spectral domain, vertical sensitivity, and treatment within the assimilation. IASI, operating in the thermal infrared (TIR) from the Metop satellites, has strongest sensitivity in the mid-troposphere, typical of TIR CO retrievals. Its data are assimilated after applying variational bias correction (VarBC) using predictors such as 1000–300 hPa thickness and thermal contrast and thinned to a horizontal resolution of 0.5°×0.5°. MOPITT, also a TIR product (on NASA's Terra platform), provides a similarly mid-tropospheric view of CO but is used without bias correction and serves as the long-term "anchor" for VarBC, chosen for its stable, multi-decadal record; it is likewise thinned to 0.5°×0.5°. In contrast, TROPOMI retrieves CO in the shortwave infrared (SWIR, 2.3 µm) aboard Sentinel-5P, providing sensitivity to the entire column with particularly valuable boundary-layer information in clear-sky land scenes. Cloudy-scene retrievals contain less sensitivity to the lower-troposphere but still add useful information, especially over ocean where clear-sky SWIR signals are too weak; for this reason, only cloudy ocean scenes are assimilated. TROPOMI data are filtered with qa_value>0.5, aggregated into model-scale super-observations to reduce representativeness errors given the native high resolution (~5.5×7 km), and are assimilated without bias correction because of their very different sensitivity characteristics compared to the TIR products.

Assimilation experiments demonstrate that the inclusion of TROPOMI significantly influences the CAMS CO analyses. On average, assimilating TROPOMI increases global CO columns by ~8%, helping to reduce the persistent low bias in CAMS relative to independent measurements. The largest improvements are found in comparisons with NDACC FTIR and IAGOS profiles, particularly in the lower and middle troposphere where SWIR sensitivity is strongest, and during pollution and biomass burning events such as the 2021 boreal fires. However, because MOPITT columns are generally lower than those from TROPOMI, the combined assimilation leads to a slight degradation in the fit to MOPITT, whereas the fit to IASI improves through smaller analysis departures. These contrasting outcomes illustrate the complementarity of the instruments: IASI and MOPITT provide stable, mid-tropospheric constraints, while TROPOMI contributes critical sensitivity to the boundary layer and cloudy scenes. When all three are assimilated together, CAMS achieves the most accurate total-column representation of CO, although sensitivity above ~500 hPa remains limited and high-altitude plume transport is less constrained.

Overall, the study highlights that each instrument plays a distinct role in constraining CO distributions: MOPITT as the stable anchor, IASI as a bias-corrected TIR product providing continuity, and TROPOMI as a high-resolution SWIR sensor adding valuable near-surface and cloud-scene information. Their combined assimilation leverages these complementary strengths to deliver improved global CO analyses.

[c] https://acp.copernicus.org/articles/22/14355/2022/

5.6. Conclusion

This study provides a comprehensive comparison of six and a half years of total column CO observations from IASI, MOPITT, and TROPOMI over the latitude range 70°S–70°N. Despite differences in their spectral domains and retrieval sensitivities, the three instruments show a high degree of consistency in both spatial and temporal CO variability. All datasets capture the major seasonal cycles and interannual fluctuations associated with biomass burning and anthropogenic emissions, with particularly strong enhancements over central Africa, South America, and Southeast Asia during their respective fire seasons.

Systematic differences were observed between the instruments, with IASI generally reporting higher CO columns than MOPITT, and TROPOMI consistently lying in between. The global mean biases indicate that IASI exceeds MOPITT by about 9%, while TROPOMI is approximately 6% lower than IASI and 3% higher than MOPITT. The largest discrepancies occur in tropical regions, probably linked to differences in vertical sensitivity and surface reflectivity between TIR (IASI, MOPITT) and SWIR (TROPOMI) measurements. Latitude- and season-dependent analyses confirm that these biases are robust and consistent through time, reflecting the complementary nature of the three datasets.

Regional trend analyses further demonstrate the reliability of these products for detecting temporal changes in CO. All three instruments capture a significant decrease in CO over the North China Plain, attributed to reduced anthropogenic emissions, and a moderate positive trend over the Amazon Basin, consistent with intensified biomass burning activity in recent years. The overall agreement in trends, despite differences in retrieval characteristics, reinforces confidence in the stability and comparability of the instruments.

In summary, IASI, MOPITT, and TROPOMI together provide a coherent and complementary view of global CO distributions. IASI and MOPITT offer long-term continuity and robust mid-tropospheric sensitivity, while TROPOMI contributes high-resolution observations with enhanced boundary-layer sensitivity. Combined use of these products, as demonstrated in both this comparison and in assimilation studies such as Inness et al. (2022), represents a powerful approach for monitoring CO variability, evaluating emission trends, and improving atmospheric reanalyses at global and regional scales.

6. References

Ainsworth, E., Yendrek, C., Sitch, S., Collins, W., and Emberson, L. : The Effects of Tropospheric Ozone on Net Primary Productivity and Implications for Climate Change, Annu. Rev. Plant Biol., 63, 637–661, https://www.annualreviews.org/doi/10.1146/annurev-arplant-042110-103829, 2012

Andreae, M. O.: Emission of trace gases and aerosols from biomass burning – an updated assessment, Atmospheric Chem. Phys., 19, 8523–8546, https://doi.org/10.5194/acp-19-8523-2019, 2019.

Atkinson, R.: Atmospheric chemistry of VOCs and NOx, Atmos. Environ., 34, 2063–2101, https://doi.org/10.1016/S1352-2310(99)00460-4, 2000.

Barret, B., Emili, E., and Le Flochmoen, E. : A tropopause-related climatological a priori profile for IASI-SOFRID ozone retrievals: improvements and validation, Atmos. Meas. Tech., 13, 5237–5257, https://doi.org/10.5194/amt-13-5237-2020 , 2020.

Barret, B., Loicq, P., Le Flochmoën, E., Bennouna, Y., Hadji-Lazaro, J., Hurtmans, D., and Sauvage, B.: Validation of 12 years (2008–2019) of IASI-A CO with IAGOS aircraft observations, Atmos. Meas. Tech., 18, 129–149, https://doi.org/10.5194/amt-18-129-2025 , 2025.

Bates DV. Ambient ozone and mortality. Epidemiology. 2005 Jul;16(4):427-9. doi : 10.1097/01.ede.0000165793.71278.ec. PMID: 15951659.

Bauwens, M., Stavrakou, T., Müller, J.-F., De Smedt, I., Van Roozendael, M., van der Werf, G. R., Wiedinmyer, C., Kaiser, J. W., Sindelarova, K., and Guenther, A.: Nine years of global hydrocarbon emissions based on source inversion of OMI formaldehyde observations, Atmospheric Chem. Phys., 16, 10133–10158, https://doi.org/10.5194/acp-16-10133-2016, 2016.

Berndt, T., Hyttinen, N., Herrmann, H., and Hansel, A.: First oxidation products from the reaction of hydroxyl radicals with isoprene for pristine environmental conditions, Commun. Chem., 2, 1–10, https://doi.org/10.1038/s42004-019-0120-9, 2019.

Bey, I., Jacob, D. J., Yantosca, R. M., Logan, J. A., Field, B. D., Fiore, A. M., Li, Q., Liu, H. Y., Mickley, L. J., & Schultz, M. G. (2001). Global modeling of tropospheric chemistry with assimilated meteorology: Model description and evaluation. *Journal of Geophysical Research:* Atmospheres, 106(D19), 23,073–23,095. https://doi.org/10.1029/2001JD000807

Boersma, K. F., Vinken, G. C. M., and Eskes, H. J.: Representativeness errors in comparing chemistry transport and chemistry climate models with satellite UV–Vis tropospheric column retrievals, Geosci. Model Dev., 9, 875–898, https://doi.org/10.5194/gmd-9-875-2016, 2016.

Bowman, H., Turnock, S., Bauer, S. E., Tsigaridis, K., Deushi, M., Oshima, N., O'Connor, F. M., Horowitz, L., Wu, T., Zhang, J., Kubistin, D., and Parrish, D. D.: Changes in anthropogenic precursor emissions drive shifts in the ozone seasonal cycle throughout the northern midlatitude troposphere, Atmos. Chem. Phys., 22, 3507–3524, https://doi.org/10.5194/acp-22-3507-2022, 2022.

Brauer, M., Amann, M., Burnett, R. T., Cohen, A., Dentener, F., Ezzati, M., Henderson, S. B., Krzyzanowski, M., Martin, R. V., Van Dingenen, R., van Donkelaar, A., and Thurston, G. D.: Exposure assessment for estimation of the global burden of disease attributable to outdoor air pollution, Environ. Sci. Technol., 46, 652–660, https://doi.org/10.1021/es2025752, 2012.

Brunekreef, B. and Holgate, S. T.: Air pollution and health, The Lancet, 360, 1233–1242, 2002.

Christiansen, A., Mickley, L. J., Liu, J., Oman, L. D., and Hu, L.: Multidecadal increases in global tropospheric ozone derived from ozonesonde and surface site observations: can models reproduce ozone trends?, Atmos. Chem. Phys., 22, 14751–14782, https://doi.org/10.5194/acp-22-14751-2022 , 2022.

Chen, Y., Turnock, S. T., Scott, C. E., and Arnold, S. R.: Radiative Response to Large Decline in Anthropogenic Emissions From China Between 2008 and 2016 Is Modified by Simultaneous Biomass Burning Emission Changes, Journal of Geophysical Research: Atmospheres, 130, e2025JD044 548, https://doi.org/https://doi.org/10.1029/2025JD044548, e2025JD044548 2025JD044548, 2025.

Claeys, M., Graham, B., Vas, G., Wang, W., Vermeylen, R., Pashynska, V., Cafmeyer, J., Guyon, P., Andreae, M., Artaxo, P., and Maenhaut, W.: Formation of Secondary Organic Aerosols Through Photooxidation of Isoprene, Science, 303, 1173–6, https://doi.org/10.1126/science.1092805, 2004.

Darmenov, A. S. and Da Silva, A.: The Quick Fire Emissions Dataset (QFED): Documentation of versions 2.1, 2.2 and 2.4., 2015.

De Smedt, I.: CCI+P HCHO tropospheric column L3 data from OMI, v2 (Version 2) [Data set] (2), https://doi.org/10.18758/BF145884, 2025.

De Wachter, E., Barret, B., Le Flochmoën, E., Pavelin, E., Matricardi, M., Clerbaux, C., Hadji-Lazaro, J., George, M., Hurtmans, D., Coheur, P.-F., Nedelec, P., and Cammas, J. P.: Retrieval of MetOp-A/IASI CO profiles and validation with MOZAIC data, Atmos. Meas. Tech., 5, 2843–2857, https://doi.org/10.5194/amt-5-2843-2012 , 2012.

Dufour, G., Eremenko, M., Griesfeller, A., Barret, B., LeFlochmoën, E., Clerbaux, C., Hadji-Lazaro, J., Coheur, P.-F., and Hurtmans, D.: Validation of three different scientific ozone products retrieved from IASI spectra using ozonesondes, Atmos. Meas. Tech., 5, 611–630, https://doi.org/10.5194/amt-5-611-2012 , 2012.

Eastham, S. D., Long, M. S., & Jacob, D. J. (2018). GEOS-Chem High Performance (GCHP v11-02c): A next-generation implementation of the GEOS-Chem chemical transport model for massively parallel applications. Geoscientific Model Development, 11(7), 2941–2953. https://doi.org/10.5194/gmd-11-2941-2018

Friedl, M. and Sulla-Menashe, D.: MCD12Q1 MODIS/Terra+Aqua Land Cover Type Yearly L3 Global 500 m SIN Grid V006 [Dataset] (NASA EOSDIS Land Processes DAAC), 2019.

Froidevaux, L., Kinnison, D. E., Gaubert, B., Schwartz, M. J., Livesey, N. J., Read, W. G., Bardeen, C. G., Ziemke, J. R., and Fuller, R. A.: Tropical upper-tropospheric trends in ozone and carbon

monoxide (2005–2020): observational and model results, Atmos. Chem. Phys., 25, 597–624, https://doi.org/10.5194/acp-25-597-2025, 2025.

Gaudel, A., Cooper, O. R., Ancellet, G., Barret, B., Boynard, A., Burrows, J. P., Clerbaux, C., Coheur, P. F., Cuesta, J., Cuevas, E., Doniki, S., Dufour, G., Ebojie, F., Foret, G., Garcia, O., Granados-Munoz, M. J., Hannigan, J. W., Hase, F., Hassler, B., Huang, G., Hurtmans, D., Jaffe, D., Jones, N., Kalabokas, P., Kerridge, B., Kulawik, S., Latter, B., Leblanc, T., Le Flochmoen, E., Lin, W., Liu, J., Liu, X., Mahieu, E., McClure-Begley, A., Neu, J. L., Osman, M., Palm, M., Petetin, H., Petropavlovskikh, I., Querel, R., Rahpoe, N., Rozanov, A., Schultz, M. G., Schwab, J., Siddans, R., Smale, D., Steinbacher, M., Tanimoto, H., Tarasick, D. W., Thouret, V., Thompson, A. M., Trickl, T., Weatherhead, E., Wespes, C., Worden, H. M., Vigouroux, C., Xu, X., Zeng, G., and Ziemke, J.: Tropospheric Ozone Assessment Report: Present-day distribution and trends of tropospheric ozone relevant to climate and global atmospheric chemistry model evaluation, Elem. Sci. Anthrop., 6, 39, https://doi.org/10.1525/elementa.291, 2018.

Geddes, J. A., Murphy, J. G., O'Brien, J. M., and Celarier, E. A.: Biases in long-term NO_2 averages inferred from satellite observations due to cloud selection criteria, Remote Sensing of Environment, 124, 210–216, https://doi.org/https://doi.org/10.1016/j.rse.2012.05.008, 2012.

Gelaro, R., et al. (2017), *The Modern-Era Retrospective Analysis for Research and Applications, Version 2 (MERRA-2)*, *Journal of Climate*, doi: 10.1175/JCLI-D-16-0758.

Glissenaar, I., Boersma, K. F., Anglou, I., Rijsdijk, P., Verhoelst, T., Compernolle, S., Pinardi, G., Lambert, J.-C., Van Roozendael, M., and Eskes, H.: TROPOMI Level 3 tropospheric NO_2 dataset with advanced uncertainty analysis from the ESA CCI+ ECV precursor project, Earth Syst. Sci. Data, 17, 4627–4650, https://doi.org/10.5194/essd-17-4627-2025, 2025.

Granier, C., Darras, S., Denier van der Gon, H., Doubalova, J., Elguindi, N., Galle, B., Gauss, M., Guevara, M., Jalkanen, J.-P., Kuenen, J., Liousse, C., Quack, B., Simpson, D., and Sindelarova, K.: The Copernicus Atmosphere Monitoring Service global and regional emissions (April 2019 version), Copernic. Atmosphere Monit. Serv., https://doi.org/10.24380/D0BN-KX16, 2019.

Guenther, A. B., Jiang, X., Heald, C. L., Sakulyanontvittaya, T., Duhl, T., Emmons, L. K., and Wang, X.: The Model of Emissions of Gases and Aerosols from Nature version 2.1 (MEGAN2.1): an extended and updated framework for modeling biogenic emissions, Geosci. Model Dev., 5, 1471–1492, https://doi.org/10.5194/gmd-5-1471-2012 , 2012.

Guenther, A., Karl, T., Harley, P., Wiedinmyer, C., Palmer, P. I., and Geron, C.: Estimates of global terrestrial isoprene emissions using MEGAN (Model of Emissions of Gases and Aerosols from Nature), Atmos. Chem. Phys., 6, 3181–3210, https://doi.org/10.5194/acp-6-3181-2006 , 2006.

Hallquist, M., Wenger, J. C., Baltensperger, U., Rudich, Y., Simpson, D., Claeys, M., Dommen, J., Donahue, N. M., George, C., Goldstein, A. H., Hamilton, J. F., Herrmann, H., Hoffmann, T., Iinuma, Y., Jang, M., Jenkin, M. E., Jimenez, J. L., Kiendler-Scharr, A., Maenhaut, W., McFiggans, G., Mentel, T. F., Monod, A., Prévôt, A. S. H., Seinfeld, J. H., Surratt, J. D., Szmigielski, R., and Wildt, J.: The formation, properties and impact of secondary organic aerosol: current and

emerging issues, Atmospheric Chem. Phys., 9, 5155–5236, https://doi.org/10.5194/acp-9-5155-2009, 2009.

Hammer, M. S., van Donkelaar, A., Li, C., Lyapustin, A., Sayer, A. M., Hsu, N. C., Levy, R. C., Garay, M. J., Kalashnikova, O. V., Kahn, R. A., Brauer, M., Apte, J. S., Henze, D. K., Zhang, L., Zhang, Q., Ford, B., Pierce, J. R., and Martin, R. V. : Global Estimates and Long-Term Trends of Fine Particulate Matter Concentrations (1998–2018), Environ. Sci. Technol., 54, 7879–7890, https://doi.org/10.1021/acs.est.0c01764 , 2020.

Hansen, M. C., Potapov, P. V., Moore, R., Hancher, M., Turubanova, S. A., Tyukavina, A., Thau, D., Stehman, S. V., Goetz, S. J., Loveland, T. R., Kommareddy, A., Egorov, A., Chini, L., Justice, C. O., and Townshend, J. R. G.: High-Resolution Global Maps of 21st-Century Forest Cover Change, Science, 342, 850–853, https://doi.org/10.1126/science.1244693, 2013.

Hersbach, H., Bell, B., Berrisford, P., Hirahara, S., Horányi, A., Muñoz-Sabater, J., Nicolas, J., Peubey, C., Radu, R., Schepers, D., Simmons, A., Soci, C., Abdalla, S., Abellan, X., Balsamo, G., Bechtold, P., Biavati, G., Bidlot, J., Bonavita, M., De Chiara, G., Dahlgren, P., Dee, D., Diamantakis, M., Dragani, R., Flemming, J., Forbes, R., Fuentes, M., Geer, A., Haimberger, L., Healy, S., Hogan, R. J., Hólm, E., Janisková, M., Keeley, S., Laloyaux, P., Lopez, P., Lupu, C., Radnoti, G., de Rosnay, P., Rozum, I., Vamborg, F., Villaume, S., and Thépaut, J.-N.: The ERA5 global reanalysis, Q. J. R. Meteorol. Soc., 146, 1999–2049, https://doi.org/10.1002/qj.3803, 2020.

Hoesly, R. M., Smith, S. J., Feng, L., Klimont, Z., Janssens Maenhout, G., Pitkanen, T., Seibert, J. J., Vu, L., Andres, R. J., Bolt, R. M., Bond, T. C., Dawidowski, L., Kholod, N., Kurokawa, J.-I., Li, M., Liu, L., Lu, Z., Moura, M. C. P., O'Rourke, P. R., and Zhang, Q.: Historical (1750–2014) anthropogenic emissions of reactive gases and aerosols from the Community Emissions Data System (CEDS), Geosci. Model Dev., 11, 369–408, https://doi.org/10.5194/gmd-11-369-2018, 2018.

Hoque, H. M. S., Sudo, K., Irie, H., He, Y., and Khan, M. F.: Evaluating CHASER V4.0 global formaldehyde (HCHO) simulations using satellite, aircraft, and ground-based remote-sensing observations, Geosci. Model Dev., 17, 5545–5571, https://doi.org/10.5194/gmd-17-5545-2024, 2024.

Hudman, R. C., Moore, N. E., Mebust, A. K., Martin, R. V., Russell, A. R., Valin, L. C., and Cohen, R. C.: Steps towards a mechanistic model of global soil nitric oxide emissions: implementation and space based-constraints, Atmos. Chem. Phys., 12, 7779–7795, https://doi.org/10.5194/acp-12-7779-2012, 2012.

IPCC: Climate Change 2007: The Physical Science Basis. Contribution of Working Group I to the Fourth Assessment Report of the Intergovernmental Panel on Climate Change. Chapter 1, Historical Overview of Climate change, in: Intergovernmental Panel on Climate Change Climate change: The Physical Science Basis, Contribution of Working Group I to the Fourth Assessment Report of the IPCC, Cambridge University Press, Cambridge, 79–131, 2007.

Jaeglé, L., Martin, R. V., Chance, K., Steinberger, L., Kurosu, T. P., Jacob, D. J., Modi, A. I., Yoboué, V., Sigha-Nkamdjou, L., and Galy-Lacaux, C.: Satellite mapping of rain-induced nitric oxide emissions from soils, J. Geophys. Res. Atmospheres, 109, https://doi.org/10.1029/2004JD004787, 2004.

Jaeglé, L., Steinberger, L., Martin, R. V., and Chance, K.: Global partitioning of NOx sources using satellite observations: Relative roles of fossil fuel combustion, biomass burning and soil emissions, Faraday Discuss., 130, 407–423, https://doi.org/10.1039/B502128F, 2005.

Jiang, Z., Zhu, R., Miyazaki, K., McDonald, B. C., Klimont, Z., Zheng, B., Boersma, K. F., Zhang, Q., Worden, H., Worden, J. R., Henze, D. K., Jones, D. B. A., Denier van der Gon, H. A. C., and Eskes, H.: Decadal Variabilities in Tropospheric Nitrogen Oxides Over United States, Europe, and China, J. Geophys. Res.-Atmos., 127, e2021JD035872, https://doi.org/10.1029/2021jd035872 , 2022

Kaiser, J. W., Heil, A., Andreae, M. O., Benedetti, A., Chubarova, N., Jones, L., Morcrette, J.-J., Razinger, M., Schultz, M. G., Suttie, M., and van der Werf, G. R.: Biomass burning emissions estimated with a global fire assimilation system based on observed fire radiative power, Biogeosciences, 9, 527–554, https://doi.org/10.5194/bg-9-527-2012, 2012.

Keller, C. A., Long, M. S., Yantosca, R. M., Da Silva, A. M., Pawson, S., and Jacob, D. J.: HEMCO v1.0: a versatile, ESMF-compliant component for calculating emissions in atmospheric models, Geosci. Model Dev., 7, 1409–1417, https://doi.org/10.5194/gmd-7-1409-2014 , 2014.

Kim, H., Park, R. J., Kim, S., Brune, W. H., Diskin, G. S., Fried, A., Hall, S. R., Weinheimer, A. J., Wennberg, P., Wisthaler, A., Blake, D. R., & Ullmann, K. (2022). Observed versus simulated OH reactivity during KORUS-AQ campaign: Implications for emission inventory and chemical environment in East Asia. *Elementa*, *10*(1), Article 00030. https://doi.org/10.1525/elementa.2022.00030

Kleipool, Q., et al. (2022), Ozone Monitoring Instrument (OMI) Collection 4: establishing a 17-year-long series of detrended Level-1b data, Atmos. Meas. Tech., 15, 3527–3545.

Kopacz, M., Jacob, D. J., Fisher, J. A., Logan, J. A., Zhang, L., Megretskaia, I. A., Yantosca, R. M., Singh, K., Henze, D. K., Burrows, J. P., Buchwitz, M., Khlystova, I., McMillan, W. W., Gille, J. C., Edwards, D. P., Eldering, A., Thouret, V., and Nedelec, P.: Global estimates of CO sources with high resolution by adjoint inversion of multiple satellite datasets (MOPITT, AIRS, SCIAMACHY, TES), Atmos. Chem. Phys., 10, 855–876, https://doi.org/10.5194/acp-10-855-2010 , 2010.

Kwan, A. J., Chan, A. W. H., Ng, N. L., Kjaergaard, H. G., Seinfeld, J. H., and Wennberg, P. O.: Peroxy radical chemistry and OH radical production during the NO_3-initiated oxidation of isoprene, Atmospheric Chem. Phys., 12, 7499–7515, https://doi.org/10.5194/acp-12-7499-2012, 2012.

Lathière, J., Hauglustaine, D. A., Friend, A. D., De Noblet-Ducoudré, N., Viovy, N., and Folberth, G. A.: Impact of climate variability and land use changes on global biogenic volatile organic

compound emissions, Atmos. Chem. Phys., 6, 2129–2146, https://doi.org/10.5194/acp-6-2129-2006 , 2006.

Levelt, P. F., et al. (2006), The Ozone Monitoring Instrument, IEEE Trans. Geosci. Remote Sens., 44(5), 1093–1101.

Levelt, P. F., et al. (2018), The Ozone Monitoring Instrument: Overview of 14 years in space, Atmos. Chem. Phys., 18, 5699–5745.

Levelt, P. F., van den Oord, G. H. J., Dobber, M. R., Malkki, A., Visser, H., Vries, J. de, Stammes, P., Lundell, J. O. V., and Saari, H.: The ozone monitoring instrument, IEEE Trans. Geosci. Remote Sens., 44, 1093–1101, https://doi.org/10.1109/TGRS.2006.872333, 2006.

Li, K., Jacob, D. J., Liao, H., Shen, L., Zhang, Q., and Bates, K. H.: Anthropogenic drivers of 2013-2017 trends in summer surface ozone in China, P. Natl. Acad. Sci. USA, 116, 422–427, https://doi.org/10.1073/pnas.1812168116 , 2019.

Lin, H., Emmons, L. K., Lundgren, E. W., Yang, L. H., Feng, X., Dang, R., Zhai, S., Tang, Y., Kelp, M. M., Colombi, N. K., Eastham, S. D., Fritz, T. M., and Jacob, D. J.: Intercomparison of GEOS-Chem and CAM-chem tropospheric oxidant chemistry within the Community Earth System Model version 2 (CESM2), Atmos. Chem. Phys., 24, 8607–8624, https://doi.org/10.5194/acp-24-8607-2024 , 2024.

Lin, H., Jacob, D. J., Lundgren, E. W., Sulprizio, M. P., Keller, C. A., Fritz, T. M., Eastham, S. D., Emmons, L. K., Campbell, P. C., Baker, B., Saylor, R. D., and Montuoro, R.: Harmonized Emissions Component (HEMCO) 3.0 as a versatile emissions component for atmospheric models: application in the GEOS-Chem, NASA GEOS, WRF-GC, CESM2, NOAA GEFS-Aerosol, and NOAA UFS models, Geosci. Model Dev., 14, 5487–5506, https://doi.org/10.5194/gmd- 14-5487-2021, 2021.

Liu, H., D. J. Jacob, I. Bey, and R. M. Yantosca (2001), Constraints from ^{210}Pb and ^{7}Be on wet deposition and transport in a global three-dimensional chemical tracer model driven by assimilated meteorological fields, J. Geophys. Res., 106(D11), 12109–12128, doi:10.1029/2000JD900839.

Ludewig, A., et al. (2020), TROPOMI – The Netherlands' Sentinel-5 Precursor contribution, Remote Sens., 12, 4133. Clerbaux, C., et al. (2009), *Monitoring of atmospheric composition using the thermal infrared IASI/MetOp sounder*, Atmos. Chem. Phys., 9, 6041–6054.

Marais, E. A., Jacob, D. J., Kurosu, T. P., Chance, K., Murphy, J. G., Reeves, C., Mills, G., Casadio, S., Millet, D. B., Barkley, M. P., Paulot, F., and Mao, J.: Isoprene emissions in Africa inferred from OMI observations of formaldehyde columns, Atmospheric Chem. Phys., 12, 6219–6235, https://doi.org/10.5194/acp-12-6219-2012, 2012.

McDuffie, E. E., Smith, S. J., O'Rourke, P., Tibrewal, K., Venkataraman, C., Marais, E. A., Zheng, B., Crippa, M., Brauer, M., and Martin, R. V.: A global anthropogenic emission inventory of atmospheric pollutants from sector- and fuel-specific sources (1970–2017): an application of

the Community Emissions Data System (CEDS), Earth System Science Data, 12, 3413–3442, https://doi.org/10.5194/essd-12-3413-2020, 2020.

Mead, M. I., Okello, G., Mbandi, A. M., and Pope, F. D.: Spotlight on air pollution in Africa, Nat. Geosci., 16, 930–931, https://doi.org/10.1038/s41561-023-01311-2, 2023.

Messina, P., Lathière, J., Sindelarova, K., Vuichard, N., Granier, C., Ghattas, J., Cozic, A., and Hauglustaine, D. A.: Global biogenic volatile organic compound emissions in the ORCHIDEE and MEGAN models and sensitivity to key parameters, Atmospheric Chem. Phys., 16, 14169–14202, https://doi.org/10.5194/acp-16-14169-2016, 2016.

Millet, D. B., Guenther, A., Siegel, D. A., Nelson, N. B., Singh, H. B., de Gouw, J. A., Warneke, C., Williams, J., Eerdekens, G., Sinha, V., Karl, T., Flocke, F., Apel, E., Riemer, D. D., Palmer, P. I., and Barkley, M.: Global atmospheric budget of acetaldehyde: 3-D model analysis and constraints from in-situ and satellite observations, Atmospheric Chem. Phys., 10, 3405–3425, https://doi.org/10.5194/acp-10-3405-2010, 2010.

Monks, PS, Archibald, AT, Colette, A, Cooper, O, Coyle, M, Derwent, R, Fowler, D, Granier, C, Law, KS, Mills, GE, Stevenson, DS, Tarasova, O, Thouret, V, von Schneidemesser, E, Sommariva, R, Wild, O and Williams, ML. 2015. Tropospheric ozone and its precursors from the urban to the global scale from air quality to short-lived climate forcer. Atmos. Chem. Phys., 15, 8889–8973, DOI: https://doi.org/10.5194/acp-15-8889-2015 , 2015.

Müller, J.-F. and Brasseur, G.: IMAGES: A three-dimensional chemical transport model of the global troposphere, J. Geophys. Res. Atmospheres, 100, 16445–16490, https://doi.org/10.1029/94JD03254, 1995.

Müller, J.-F. and Stavrakou, T.: Inversion of CO and NO_x emissions using the adjoint of the IMAGES model, Atmospheric Chem. Phys., 5, 1157–1186, https://doi.org/10.5194/acp-5-1157-2005, 2005.

Müller, J.-F., Peeters, J., and Stavrakou, T.: Fast photolysis of carbonyl nitrates from isoprene, Atmospheric Chem. Phys., 14, 2497–2508, https://doi.org/10.5194/acp-14-2497-2014, 2014.

Müller, J.-F., Stavrakou, T., and Peeters, J.: Chemistry and deposition in the Model of Atmospheric composition at Global and Regional scales using Inversion Techniques for Trace gas Emissions (MAGRITTE v1.1) – Part 1: Chemical mechanism, Geosci. Model Dev., 12, 2307–2356, https://doi.org/10.5194/gmd-12-2307-2019, 2019.

Murray, L. T., Jacob, D. J., Logan, J. A., Hudman, R. C., and Koshak, W. J.: Optimized regional and interannual variability of lightning in a global chemical transport model constrained by LIS/OTD satellite data, J. Geophys. Res., 117,D20307, https://doi.org/10.1029/2012JD017934 , 2012

Nguyen, T. B., Crounse, J. D., Teng, A. P., St Clair, J. M., Paulot, F., Wolfe, G. M., and Wennberg, P. O.: Rapid deposition of oxidized biogenic compounds to a temperate forest, Proc. Natl. Acad. Sci. U. S. A., 112, E392-401, https://doi.org/10.1073/pnas.1418702112, 2015.

Opacka, B., Müller, J.-F., Stavrakou, T., Bauwens, M., Sindelarova, K., Markova, J., and Guenther, A. B.: Global and regional impacts of land cover changes on isoprene emissions

derived from spaceborne data and the MEGAN model, Atmospheric Chem. Phys., 21, 8413–8436, https://doi.org/10.5194/acp-21-8413-2021, 2021.

Opacka, B., Stavrakou, T., Müller, J.-F., De Smedt, I., van Geffen, J., Marais, E. A., Horner, R. P., Millet, D. B., Wells, K. C., and Guenther, A. B.: Natural emissions of VOC and NO_x over Africa constrained by TROPOMI HCHO and NO_2 data using the MAGRITTEv1.1 model, Atmospheric Chem. Phys., 25, 2863–2894, https://doi.org/10.5194/acp-25-2863-2025, 2025.

Pan, X., Ichoku, C., Chin, M., Bian, H., Darmenov, A., Colarco, P., Ellison, L., Kucsera, T., da Silva, A., Wang, J., Oda, T., and Cui, G.: Six global biomass burning emission datasets: intercomparison and application in one global aerosol model, Atmospheric Chem. Phys., 20, 969–994, https://doi.org/10.5194/acp-20-969-2020, 2020.

Park, R. J., Jacob, D. J., Field, B. D., et al. (2004). Natural and transboundary pollution influences on sulfate–nitrate–ammonium aerosols in the United States. Journal of Geophysical Research, 109, D15204. https://doi.org/10.1029/2003JD004473

Paulot, F., Crounse, J. D., Kjaergaard, H. G., Kroll, J. H., Seinfeld, J. H., and Wennberg, P. O.: Isoprene photooxidation: new insights into the production of acids and organic nitrates, Atmospheric Chem. Phys., 9, 1479–1501, https://doi.org/10.5194/acp-9-1479-2009, 2009.

Peeters, J., Müller, J.-F., Stavrakou, T., and Nguyen, V. S.: Hydroxyl Radical Recycling in Isoprene Oxidation Driven by Hydrogen Bonding and Hydrogen Tunneling: The Upgraded LIM1 Mechanism, J. Phys. Chem. A, 118, 8625–8643, https://doi.org/10.1021/jp5033146, 2014.

Petkova, E., Jack, D., Volavka-Close, N., and Kinney, P.: Particulate matter pollution in African cities, Air Qual. Atmosphere Health, 6, https://doi.org/10.1007/s11869-013-0199-6, 2013.

Pope, R. J., Rap, A., Pimlott, M. A., Barret, B., Le Flochmoen, E., Kerridge, B. J., Siddans, R., Latter, B. G., Ventress, L. J., Boynard, A., Retscher, C., Feng, W., Rigby, R., Dhomse, S. S., Wespes, C., and Chipperfield, M. P.: Quantifying the tropospheric ozone radiative effect and its temporal evolution in the satellite era, Atmos. Chem. Phys., 24, 3613–3626, https://doi.org/10.5194/acp-24-3613-2024 , 2024.

Romer, P. S., Duffey, K. C., Wooldridge, P. J., Allen, H. M., Ayres, B. R., Brown, S. S., Brune, W. H., Crounse, J. D., de Gouw, J., Draper, D. C., Feiner, P. A., Fry, J. L., Goldstein, A. H., Koss, A., Misztal, P. K., Nguyen, T. B., Olson, K., Teng, A. P., Wennberg, P. O., Wild, R. J., Zhang, L., and Cohen, R. C.: The lifetime of nitrogen oxides in an isoprene-dominated forest, Atmospheric Chem. Phys., 16, 7623–7637, https://doi.org/10.5194/acp-16-7623-2016, 2016.

Ryerson, T. B., Trainer, M., Holloway, J. S., Parrish, D. D., Huey, L. G., Sueper, D. T., Frost, G. J., Donnelly, S. G., Schauffler, S., Atlas, E. L., Kuster, W. C., Goldan, P. D., Hübler, G., Meagher, J. F., and Fehsenfeld, F. C.: Observations of Ozone Formation in Power Plant Plumes and Implications for Ozone Control Strategies, Science, 292, 719–723, https://doi.org/10.1126/science.1058113, 2001.

Saunier, A., Ormeño, E., Piga, D., Armengaud, A., Boissard, C., Lathière, J., Szopa, S., Genard-Zielinski, A.-C., and Fernandez, C.: Isoprene contribution to ozone production under climate change conditions in the French Mediterranean area, Reg. Environ. Change, 20, 111, https://doi.org/10.1007/s10113-020-01697-4, 2020.

Sauvage, B., Martin, R. V., van Donkelaar, A., Liu, X., Chance, K., Jaeglé, L., Palmer, P. I., Wu, S., and Fu, T.-M.: Remote sensed and in situ constraints on processes affecting tropical tropospheric ozone, Atmos. Chem. Phys., 7, 815–838, https://doi.org/10.5194/acp-7-815-2007 , 2007

Sherwen, T., Evans, M. J., Carpenter, L. J., et al. (2016). Effects of halogens on European air-quality. Faraday Discussions, 189, 589–616. https://doi.org/10.1039/C5FD00026J

Shindell, D. T., Faluvegi, G., and Stevenson, D. S. E. A.: Multimodel simulations of carbon monoxide: Comparison with observations and projected near-future changes, J. Geophys. Res.-Atmos., 111, D19306, https://doi.org/10.1029/2006jd007100 , 2006.

Sindelarova, K., Granier, C., Bouarar, I., Guenther, A., Tilmes, S., Stavrakou, T., Müller, J.-F., Kuhn, U., Stefani, P., and Knorr, W.: Global data set of biogenic VOC emissions calculated by the MEGAN model over the last 30 years, Atmospheric Chem. Phys., 14, 9317–9341, https://doi.org/10.5194/acp-14-9317-2014, 2014.

Sindelarova, K., Markova, J., Simpson, D., Huszar, P., Karlicky, J., Darras, S., and Granier, C.: High-resolution biogenic global emission inventory for the time period 2000–2019 for air quality modelling, Earth Syst. Sci. Data, 14, 251–270, https://doi.org/10.5194/essd-14-251-2022, 2022.

Singh, A., Avis, W. R., and Pope, F. D.: Visibility as a proxy for air quality in East Africa, Environ. Res. Lett., 15, 084002, https://doi.org/10.1088/1748-9326/ab8b12, 2020.

Soulie, A., Granier, C., Darras, S., Zilbermann, N., Doumbia, T., Guevara, M., Jalkanen, J.-P., Keita, S., Liousse, C., Crippa, M., Guizzardi, D., Hoesly, R., and Smith, S. J.: Global anthropogenic emissions (CAMS-GLOB-ANT) for the Copernicus Atmosphere Monitoring Service simulations of air quality forecasts and reanalyses, Earth Syst. Sci. Data, 16, 2261–2279, https://doi.org/10.5194/essd-16-2261-2024, 2024.

Stavrakou, T., Müller, J.-F., Bauwens, M., De Smedt, I., Van Roozendael, M., De Mazière, M., Vigouroux, C., Hendrick, F., George, M., Clerbaux, C., Coheur, P.-F., and Guenther, A.: How consistent are top-down hydrocarbon emissions based on formaldehyde observations from GOME-2 and OMI?, Atmospheric Chem. Phys., 15, 11861–11884, https://doi.org/10.5194/acp-15-11861-2015, 2015.

Stavrakou, T., Müller, J.-F., Bauwens, M., De Smedt, I., Van Roozendael, M., and Guenther, A.: Impact of Short-Term Climate Variability on Volatile Organic Compounds Emissions Assessed Using OMI Satellite Formaldehyde Observations, Geophys. Res. Lett., 45, 8681–8689, https://doi.org/10.1029/2018GL078676, 2018.

Stavrakou, T., Müller, J.-F., Boersma, K. F., van der A, R. J., Kurokawa, J., Ohara, T., and Zhang, Q.: Key chemical NO_x sink uncertainties and how they influence top-down emissions of nitrogen oxides, Atmospheric Chem. Phys., 13, 9057–9082, https://doi.org/10.5194/acp-13-9057-2013, 2013.

Stavrakou, T., Müller, J.-F., De Smedt, I., Van Roozendael, M., van der Werf, G. R., Giglio, L., and Guenther, A.: Global emissions of non-methane hydrocarbons deduced from SCIAMACHY

formaldehyde columns through 2003–2006, Atmospheric Chem. Phys., 9, 3663–3679, https://doi.org/10.5194/acp-9-3663-2009, 2009.

Stevenson, D. S., Young, P. J., Naik, V., Lamarque, J.-F., Shindell, D. T., Voulgarakis, A., Skeie, R. B., Dalsoren, S. B., Myhre, G., Berntsen, T. K., Folberth, G. A., Rumbold, S. T., Collins, W. J., MacKenzie, I. A., Doherty, R. M., Zeng, G., van Noije, T. P. C., Strunk, A., Bergmann, D., Cameron-Smith, P., Plummer, D. A., Strode, S. A., Horowitz, L., Lee, Y. H., Szopa, S., Sudo, K., Nagashima, T., Josse, B., Cionni, I., Righi, M., Eyring, V., Conley, A., Bowman, K. W., Wild, O., and Archibald, A.: Tropospheric ozone changes, radiative forcing and attribution to emissions in the Atmospheric Chemistry and Climate Model Intercomparison Project (ACCMIP), Atmos. Chem. Phys., 13, 3063–3085, doi:10.5194/acp-13-3063-2013, 2013.

van der Werf, G. R., Randerson, J. T., Giglio, L., van Leeuwen, T. T., Chen, Y., Rogers, B. M., Mu, M., van Marle, M. J. E., Morton, D. C., Collatz, G. J., Yokelson, R. J., and Kasibhatla, P. S.: Global fire emissions estimates during 1997–2016, Earth Syst. Sci. Data, 9, 697–720, https://doi.org/10.5194/essd-9-697-2017, 2017.

Veefkind, J. P., et al. (2012), TROPOMI on the ESA Sentinel-5 Precursor: A GMES mission for global observations of the atmospheric composition for climate, air quality, and ozone layer applications, Remote Sens. Environ., 120, 70–83.

Wang, H., Lu, X., Jacob, D. J., Cooper, O. R., Chang, K.-L., Li, K., Gao, M., Liu, Y., Sheng, B., Wu, K., Wu, T., Zhang, J., Sauvage, B., Nédélec, P., Blot, R., and Fan, S.: Global tropospheric ozone trends, attributions, and radiative impacts in 1995–2017: an integrated analysis using aircraft (IAGOS) observations, ozonesonde, and multi-decadal chemical model simulations, Atmos. Chem. Phys., 22, 13753–13782, https://doi.org/10.5194/acp-22-13753-2022 , 2022.

Wang, Y., Li, K., Chen, X., Yang, Z., Tang, M., Campos, P. M. D., Yang, Y., Yue, X., and Liao, H.: Revisiting the high tropospheric ozone over southern Africa: role of biomass burning and anthropogenic emissions, Atmos. Chem. Phys., 25, 4455–4475, https://doi.org/10.5194/acp-25-4455-2025, 2025.

Wells, K. C., Millet, D. B., Payne, V. H., Deventer, M. J., Bates, K. H., de Gouw, J. A., Graus, M., Warneke, C., Wisthaler, A., and Fuentes, J. D.: Satellite isoprene retrievals constrain emissions and atmospheric oxidation, Nature, 585, 225–233, https://doi.org/10.1038/s41586-020-2664-3, 2020.

Weng, H., Lin, J., Martin, R., Millet, D. B., Jaeglé, L., Ridley, D., Keller, C., Li, C., Du, M., and Meng, J.: Global high-resolution emissions of soil NO x , sea salt aerosols, and biogenic volatile organic compounds, Sci. Data, 7, 148, https://doi.org/10.1038/s41597-020-0488-5, 2020.

Wennberg, P. O., Bates, K. H., Crounse, J. D., Dodson, L. G., McVay, R. C., Mertens, L. A., Nguyen, T. B., Praske, E., Schwantes, R. H., Smarte, M. D., St Clair, J. M., Teng, A. P., Zhang, X., and Seinfeld, J. H.: Gas-Phase Reactions of Isoprene and Its Major Oxidation Products, Chem. Rev., 118, 3337–3390, https://doi.org/10.1021/acs.chemrev.7b00439, 2018.

Wesely, M. L. (1989), Parameterization of surface resistances to gaseous dry deposition in regional-scale numerical models, Atmos. Environ., 23(6), 1293–1304. https://doi.org/10.1016/0004-6981(89)90153-4

Wespes, C., Hurtmans, D., Emmons, L. K., Safieddine, S., Clerbaux, C., Edwards, D. P., and Coheur, P.-F.: Ozone variability in the troposphere and the stratosphere from the first 6 years of IASI observations (2008–2013), Atmos. Chem. Phys., 16, 5721–5743, https://doi.org/10.5194/acp-165721-2016 , 2016.

Whaley, C. H., Strong, K., Jones, D. B. A., Walker, T. W., Jiang, Z., Henze, D. K., Cooke, M. A., McLinden, C. A., Mittermeier, R. L., Pommier, M., and Fogal, P. F.: Toronto area ozone: Long-term measurements and modeled sources of poor air quality events, J. Geophys. Res.-Atmos., 120, 11368–11390, https://doi.org/10.1002/2014JD022984 , 2015.

WHO : Health Aspects of Air Pollution with Particulate Matter, Ozone and Nitrogen Dioxide, Bonn, 2003.

Wiedinmyer, C., Akagi, S. K., Yokelson, R. J., Emmons, L. K., Al-Saadi, J. A., Orlando, J. J., and Soja, A. J.: The Fire INventory from NCAR (FINN): a high resolution global model to estimate the emissions from open burning, Geosci. Model Dev., 4, 625–641, https://doi.org/10.5194/gmd-4-625-2011 , 2011.

Wiedinmyer, C., Kimura, Y., McDonald-Buller, E. C., Emmons, L. K., Buchholz, R. R., Tang, W., Seto, K., Joseph, M. B., Barsanti, K. C., Carlton, A. G., and Yokelson, R.: The Fire Inventory from NCAR version 2.5: an updated global fire emissions model for climate and chemistry applications, Geosci. Model Dev., 16, 3873–3891, https://doi.org/10.5194/gmd-16-3873-2023, 2023.

Yienger, J. J. and Levy, H.: Empirical model of global soil-biogenic NOχ emissions, J. Geophys. Res. Atmospheres, 100, 11447–11464, https://doi.org/10.1029/95JD00370, 1995.

Zhang, Y, Cooper, OR, Gaudel, A, Thompson, AM, Nédélec, P, Ogino, S-Y and West, JJ. Tropospheric ozone changes from 1980 to 2010 dominated by equatorward redistribution of emissions. Nature Geosci., 9, 875–879, https://doi.org/10.1038/ngeo2827 , 2016